Dual action of sphinganine in the plant disease resistance to bacteria

Huby Eloïse[1,2], Villaume Sandra[1], Chemotti Catherine[2], Dorey Stéphan[1], Cordelier Sylvain[1], Crouzet Jérôme[1], Gilliard Guillaume[2], Terryn Christine[3], Berquand Alexandre [4], Herrfurth Cornelia[5,6], Feussner Ivo[5,6,7], Jacquard Cédric[1], Fontaine Florence[1], Clément Christophe[1], Baillieul Fabienne[1], Deleu Magali[2*], Dhondt-Cordelier Sandrine[1*]

[1]Université de Reims Champagne-Ardenne, INRAE, RIBP USC 1488, 51100 Reims, France.
[2]Laboratoire de Biophysique Moléculaire aux Interfaces (LBMI), Gembloux Agro-Bio Tech, Université de Liège, 2 Passage des déportés, 5030 Gembloux, Belgium.
[3]Université de Reims Champagne-Ardenne, PICT Platform, 51100 Reims, France.
[4]Université de Reims Champagne-Ardenne, NanoMat' Platform, 51100 Reims, France.
[5]University of Goettingen, Albrecht-von-Haller-Institute for Plant Sciences, Department of Plant Biochemistry, Justus-von-Liebig-Weig 11, D-37077, Goettingen, Germany.
[6]University of Goettingen, Goettingen Center for Molecular Biosciences (GZMB), Service Unit for Metabolomics and Lipidomics, Justus-von-Liebig-Weg 11, D-37077, Goettingen, Germany.
[7]University of Goettingen, Goettingen Center for Molecular Biosciences (GZMB), Department of Plant Biochemistry, Justus-von-Liebig-Weg 11, D-37077, Goettingen, Germany.

* MD and SDC contributed equally

Abstract

Sphingolipids are ubiquitous, highly diverse molecules constituting at least 40% of plant plasma membranes. Initially known as modulators of membrane integrity, they now emerge as important players in plant responses to (a)biotic stresses. The interaction between *Arabidopsis thaliana* and the bacterium *Pseudomonas syringae* pv. *tomato* DC3000 *AvrRpm1* (*Pst AvrRpm1*) culminates in the activation of a programmed cell death known as the hypersensitive response (HR), which is part of the plant immune response. In this study, we showed that the co-infiltration of *Pst AvrRpm1* and sphinganine (d18:0) in *Arabidopsis* leaves suppress the HR. This suppression phenotype is also observed with bacteria carrying the effectors AvrB and AvrPphB but not with the ones carrying AvrRpt2 and AvrRps4. Sphingolipid-induced HR suppression by *Pst AvrRpm1* is correlated with the down-regulation of the gene *AtNMT1* encoding a *N*-myristoyltransferase. d18:0 does not have a direct antibacterial

effect and its co-infiltration in plants does not display typical signs of immune response such as activation of salicylic acid signaling pathway and extracellular reactive oxygen species production. Biophysical studies showed that d18:0 interacts with plant plasma membrane lipids. More specifically, d18:0 disturbs plant plasma membrane organization and mechanical properties. Our results demonstrate that sphingolipids play an important role in plant resistance, especially by interfering with the plasma membrane organization and effector localization and thus disturbing their function and subsequent immune responses.

48 **1. Introduction**

49 Recognition of pathogenic microorganisms leading to plant immunity is commonly
50 divided into two pathways that can mutually potentiate each other (Ngou et al., 2021).
51 Pathogen perception involves the recognition of pathogen-associated molecular
52 patterns (PAMPs) through plant cell surface-anchored pattern recognition receptors
53 (PRRs), which induces pattern-triggered immunity (PTI) (Saijo and Loo, 2020).
54 However, some bacteria can interfere with PTI by delivering effectors into the plant cell
55 to block signaling mechanisms at different steps (Desveaux et al., 2006; Kamoun,
56 2006; Dodds et al., 2009). The recognition of microbial effectors or virulence factors by
57 the plant cells through intracellular nucleotide-binding leucine-rich repeat receptors
58 (NLRs) induces effector-triggered immunity (ETI). PTI and ETI share many signals and
59 components, but their signaling pathways are induced at different scales and time
60 (Bjornson and Zipfel, 2021; Kadota *et al*., 2019; Yuan *et al*., 2021). Typical overlaps in
61 signaling components are e.g., the production of reactive oxygen species (ROS), the
62 influx of calcium, and mitogen-activated protein kinase (MAPK) signaling cascades.
63 They also share some immune responses, such as transcriptional reprogramming and
64 alterations in stress-related hormone homeostasis, including salicylic acid (SA),
65 jasmonic acid (JA), and/or ethylene (ET) (Bari and Jones, 2009; Betsuyaku *et al*., 2018;
66 Guan *et al*., 2015). Rapid programmed cell death (PCD) at the site of infection, known
67 as the hypersensitive response (HR), usually is a hallmark of the ETI pathway (Couto
68 and Zipfel, 2016; Henry *et al*., 2013; Kadota *et al*., 2019; Ngou *et al*., 2021; Yuan *et al*.,
69 2021).

70 The bacterial pathogen *Pseudomonas syringae* pv. *tomato* DC3000 (*Pst* DC3000) has
71 been extensively studied due to its capacity to cause bacterial speck in both tomato
72 and *Arabidopsis thaliana* (hereafter *Arabidopsis*) (Lee *et al*., 2015; Wei *et al*., 2018),

73 as well as the availability of its complete genome sequence (Buell *et al*., 2003).
74 Transformation of *Pst* DC3000 to express effectors has been essential for the
75 discovery of mechanisms associated with ETI (Boyle and Martin, 2015; Hicks and
76 Galán, 2013; Nimchuk *et al*., 2000). AvrRpm1 effector was originally identified in *P.*
77 *syringae* pv. *maculicola* strain m2 (Debener *et al*., 1991) and harbors an N-terminal
78 eukaryotic consensus site for myristoylation required for its full avirulence function. This
79 allows the effector, once acylated by the plant host, to be redirected to the plant plasma
80 membrane (PM) (Boyle and Martin, 2015; Hicks and Galán, 2013; Nimchuk *et al*.,
81 2000). Although the host acylation apparatus is initially exploited by bacteria to interfere
82 with PTI by binding to the kinase domain of PRRs (Boyle and Martin, 2015), in resistant
83 plants, it can actually turn against the pathogen. For instance, in *Arabidopsis*, the NLR
84 RPM1 (RESISTANCE TO *PSEUDOMONAS SYRINGAE* PV *MACULICOLA*) is
85 monitored by the PM-associated protein RPM1-INTERACTING PROTEIN-4 (RIN4),
86 which guards it against effector-mediated perturbations (Boyes *et al*., 1998; Jones and
87 Dangl, 2006; Mackey *et al*., 2002). Therefore, once relocated to the PM, AvrRpm1 will
88 target RIN4, inducing its phosphorylation. This activates RPM1 which triggers the ETI
89 and the HR, together interrupting the spread of the bacteria and leading to the
90 degradation of RPM1 (Boyes *et al*., 1998; Mackey *et al*., 2002; Xin *et al*., 2018).
91 Sphinganine is a sphingolipid (SL), belonging to the long-chain base (LCB) class,
92 which are one major building block of SLs (Pata *et al*., 2010). It consists of a C18 core
93 with an amino group at C2 and two hydroxylations at C2 and C3 (Luttgeharm *et al*.,
94 2016; Mamode Cassim *et al*., 2019). SLs are key components of the plant PM
95 structure, accounting for up to 40 mol% of its external leaflet (Cacas *et al*., 2016). They
96 are found mostly in lipid microdomains, and play an important part in signaling, protein
97 aggregation, and stress response (Cacas *et al*., 2016; Grennan, 2007; Mamode

98 Cassim *et al*., 2019; Pata *et al*., 2010). Recent studies have shown that SLs are key
99 players in PCD regulation occurring either during plant development or immunity (Ali
100 *et al*., 2018; Berkey *et al*., 2012; Huby *et al*., 2020; Lenarčič *et al*., 2017). For instance,
101 Bax-inhibitor-1 interacts with enzymes of the SL biosynthetic pathway FAH1 and 2
102 (FATTY ACID HYDROXYLASE 1 and 2). It leads to changes in lipid content of
103 membrane microdomains (Lenarčič et al., 2017). This causes the loss of proteins
104 normally located in these microdomains and that are essential for plant defense,
105 especially for cell death by oxidative stress or SA (Ishikawa *et al*., 2015). Further links
106 between PCD, sphingolipids and the SA pathway have recently been highlighted. In
107 *Arabidopsis*, triple mutations of enzymes of the SL biosynthetic pathway, FAH1, FAH2
108 and LOH2 (LAG ONE HOMOLOG 2) led to the accumulation of sphinganine and
109 ceramides, another class of SLs. These mutants also exhibited a PCD that was
110 dependent on SA and was probably linked to d18:0 accumulation (König *et al*., 2021,
111 2012).
112 Sensing of pathogen-derived lipid molecules is far from being elucidated. A recent
113 study demonstrated that the clivage product of the *Phytophthora infestans* ceramide D
114 by the neutral ceramidase 2 is recognize by the PRR RESISTANT TO DFPM-
115 INHIBITION OF ABSCISSIC ACID SIGNALING 2 (RDA2) (Kato *et al*., 2022). Some
116 studies suggest that lipidic elicitors can directly interact with lipids in the plant PMs
117 (Cordelier *et al*., 2021). For instance, ergosterol, the main sterol of fungi, is described
118 as a general elicitor of plant defenses (Klemptner *et al*., 2014). Due to its lipidic nature
119 and its capacity to form rafts, it is thought to interact with the PM. In *Beta vulgaris,* it
120 can inhibit its H^+-ATPase activity, supposedly by tempering with the NADPH oxidase
121 present in the plant microdomains (Hao *et al*., 2014; Rossard *et al*., 2010).

122 While there are abundant reports on the links between LCBs and PCD (Ali *et al*., 2018;
123 Huby *et al*, 2020), only few data on the use of exogenously applied LCBs and their
124 mode of action are available (Glenz *et al*., 2019; Gutiérrez-Nájera *et al*., 2020; Magnin-
125 Robert *et al*., 2015; Peer *et al*., 2011; Saucedo-García *et al*., 2011, 2023; Shi *et al*.,
126 2007). In previous studies, we and others showed that the co-infiltration of *Arabidopsis*
127 leaves with an LCB and *Pst AvrRpm1* does not induce an HR (Glenz *et al*., 2022;
128 Magnin-Robert *et al*., 2015). In order to decipher the underlying mechanism, activation
129 of canonical defense responses and antibacterial effect of the LCB were analyzed.
130 Moreover, we showed similar phenotype with other effectors that share the
131 myristoylation sequence with AvrRpm1. Finally, biophysical analyses demonstrated
132 that sphinganine can interact with the plant biomimetic PM and disturb its organization
133 as well as its mechanical features.
134

135 ## 2. Material and methods

136 ### 2.1 Plant material and growth conditions

137 Seeds of the *Arabidopsis* T-DNA insertion mutants *rpm1-3* (CS68739), *rpm1-rps2-rin4*
138 (CS68760), and transgenic line *RPM1-myc rpm1* (CS68778) were obtained from the
139 Nottingham *Arabidopsis* Stock Center (http://Arabidopsis.info). Mutants, transgenic lines and
140 wild-type seeds Columbia-0 (Col-0) were grown in soil under 12 h-light/12 h-dark conditions
141 (150 µmol/m^2/s, 20°C, and 60% humidity) for 5 weeks.

142

143 ### 2.2 Chemicals

144 Sphinganine (d18:0), palmitoyl-2-linoleoyl-*sn*-glycero-3-phosphocholine (PLPC), sitosterol
145 (sito), *D*-glucosyl-ß-1,1′-*N*-palmitoyl-*D*-erythro-sphingosine (d18:1/16:0 - GluCer or
146 Glucosylceramide) were purchased from Avanti Polar Lipids. Sphingolipids were dissolved in
147 ethanol (100%); PLPC, sitosterol and GluCer were dissolved in chloroform/methanol (2:1, v:v),
148 and used without further purification. Protamine sulphate was purchased from Sigma-Aldrich
149 (France).

150

151 ### 2.3 Bacterial cultures and inoculations

152 *Pst* DC3000 strains transformed to express the effectors AvrRpm1 (*Pst AvrRpm1*), AvrRpt2
153 (*Pst AvrRpt2*), AvrRps4 (*Pst AvrRps4*), AvrB (*Pst AvrB*) or AvrPphB (*Pst AvrPphB*) were
154 provided by Prof. Jeff Dangl (University of North Carolina, USA) and Dr. Farid El-Kasmi
155 (University of Tübingen, Germany), Prof. Brian Staskawicz (University of California, USA),
156 Prof. Jane Parker (Max-Planck Institute, Cologne, Germany) and Dr. Brad Day (Michigan State
157 university, USA), respectively. Bacteria were cultured overnight under agitation (180 rpm) at
158 28°C in liquid King's B medium, supplemented with rifampicin (50 µg/mL) and kanamycin (50
159 µg/mL). Bacterial cells were collected by centrifugation, washed twice, and resuspended in 10
160 mM $MgCl_2$. Bacterial solutions were infiltrated at 10^7 CFU/mL on the abaxial side of *Arabidopsis*
161 leaves using a 1 mL syringe without needle. Co-treatment of bacteria with 100 µM d18:0 was

162 performed likewise. Control inoculations were conducted with 10 mM $MgCl_2$. At least four
163 leaves per plant were treated for each condition, with a minimum of three different plants.
164
165 **2.4 *In vitro* antibacterial assays**
166 Bacteria were cultured as previously described before being distributed in 96 wells plates at
167 10^7 CFU/mL in King's B medium supplemented with appropriate antibiotics, under agitation
168 and at 28°C. Bacteria were plated either alone, with ethanol (0.1%, v/v) or with d18:0 (100 µM).
169 OD_{600} measurements were performed using the TECAN Spark® (USA) absorbance reader,
170 every hour for 50 h. The presented data are obtained from growth curve experiments, from
171 which the growth rate was extracted.
172
173 **2.5 Pathogen assay *in planta***
174 For bacterial count experiments, bacterial cells were cultured and inoculated as described.
175 Four inoculated leaves were weighed and ground in 1 mL of 10 mM $MgCl_2$ using a mortar and
176 pestle. Appropriate dilutions were plated on King's B medium with suitable antibiotics, and
177 bacterial colonies were counted. Data are reported as means ±SD of the log (CFU/mg fresh
178 weight) of three replicates.
179
180 **2.6 RNA extraction and qRT-PCR**
181 For total RNA extraction, at least 3 leaves from 3 different inoculated plants were collected 6
182 and 48 hours post infection (hpi). Fresh material was flash-frozen in liquid nitrogen and stored
183 at -80°C until further use. RNA isolation was subsequently performed with Extract-all from
184 Eurobio Scientific (France), following recommendations from the manufacturer. For qRT-PCR,
185 1 µg RNA was used for reverse transcription using the Verso cDNA synthesis kit from Thermo
186 Fisher Scientific (USA) following the supplier's recommendations. The transcripts were then
187 quantified by qRT-PCR with a thermocycler CFX96 Real-Time system (Bio-Rad, USA) and the
188 Absolute Blue SYBR Green Master Mix (Thermo Fisher Scientific, USA). Gene-specific primers
189 were designed for PATHOGENESIS RELATED GENE 1 (*PR1)*, VEGETATIVE STORAGE

190 PROTEIN 1 (*VSP1*) and N-MYRISTOYLTRANSFERASE 1 (*NMT1*) are available in the
191 supplemental data. For each experiment, PCR was performed in triplicates. Transcript levels
192 were normalized against those of the UBIQUITIN5 (*UBQ5*) gene, used as an internal control.
193 Fold induction compared with untreated sample was calculated using the $2^{-\Delta\Delta Ct}$ method, where
194 ΔΔCt=
195 $(Ct_{GI[unknown\ sample]}-Ct_{GI[reference\ sample]})-(Ct_{UBQ5[unknown\ sample]}-Ct_{UBQ5[reference\ sample]})$
196 where GI is the gene of interest. Data were analyzed with Bio-Rad CFX Manager software v2.0
197 (Bio-Rad, USA).
198
199 **2.7 Immunoblotting assay**
200 Extraction of total proteins was performed on pre-treated leaves of *RPM1-myc rpm1* plants
201 collected 0, 2, 6 and 24 hpi. To that end, 20 mg of leaf tissue were ground in a Potter-Elvehjem
202 homogenizer with 40 µL of extraction buffer (0.35 M Tris-HCl (pH 6.8), 30% (v/v) glycerol, 10%
203 (v/v) SDS, 0.6 M DTT, 0.012% (w/v) bromophenol blue) and were denatured for 7 min at 95°C.
204 Next, samples were centrifuged at 11 000 g for 5 min and 30 µL of supernatant were separated
205 by 12% SDS-PAGE. Proteins were transferred onto PVDF membranes for 10 min at 25 V using
206 iBLOT gel transfer system (Invitrogen, France). After 30 min in 5% saturation solution (50 g/L
207 milk, TBS (137 mM NaCl, 2.7 mM KCl, 25 mM Tris-HCl), Tween20 0.05% (v/v)) and 3 times
208 for 5 min in 0.5% washing solution (5 g/L milk, TBS (137 mM NaCl, 2.7 mM KCl, 25 mM Tris-
209 HCl), Tween 20 0.05% (v/v)), membranes were incubated overnight with recombinant
210 monoclonal Anti-c-myc epitope tag [Clone 9E10] Mouse IgG1 kappa (Cliniscience, France,
211 1:1000) at 4°C. Then, membranes were washed 3 times for 5 min with the washing solution
212 and incubated 1 h with anti-mouse IgG HRP-conjugated secondary antibodies (Bio-Rad, USA,
213 1:3000) at room temperature. Finally, washed membranes were developed with SuperSignal®
214 West Femto using an Odyssey scanner (ODYSSEY® Fc Dual-Mode Imaging System, LI-COR,
215 USA).
216 To normalize protein loading, membranes were stripped 15 min with 0.25 M NaOH, blocked
217 30 min in 5% non-fat milk. Then, membranes were incubated at room temperature for 1 h with

218 plant monoclonal anti-actin primary antibodies (CusAb, USA, 1:1000) and 1 h with anti-mouse
219 IgG HRP-conjugated secondary antibodies (Cell Signalling, 1:3000). Membranes were washed
220 and developed as previously described.
221
222 **2.8 Electrolyte leakage**
223 10 min after bacteria inoculation, performed as previously described, 9-mm-diameter leaf discs
224 were collected using a cork borer from the infected area and washed extensively with distilled
225 water for 1 hour. Two leaf discs were placed in each well of a 24-well plate containing 1 mL of
226 distilled water. Conductivity measurements were then conducted over time using a B-771
227 LaquaTwin (Horiba) conductivity meter. Control inoculations were conducted with 10 mM
228 $MgCl_2$ and ethanol (0.1%, v/v).
229
230 **2.9 Extracellular ROS production**
231 Measurements of extracellular ROS production were adapted from Smith and Heese (2014).
232 Briefly, single half leaf discs (9 mm diameter) were placed in wells of a 96-well plate containing
233 150 mL of distilled water and incubated overnight at room temperature. Just before ROS
234 quantification, distilled water was replaced by 150 mL of an elicitation solution containing 20
235 mg/mL horseradish peroxidase, 0.2 mM luminol, and bacteria. Bacteria were added to a final
236 concentration of 10^8 or 10^9 CFU/mL, as specified further. In tests involving d18:0, the molecule
237 was added at a final concentration of 100 µM concomitantly with the elicitation solution. Control
238 inoculations were conducted with 10 mM $MgCl_2$ and ethanol (0.1%, v/v).
239
240 **2.10 Phytohormone and camalexin quantifications**
241 The quantification of SA, JA-isoleucine (JA-Ile) and camalexin was performed at 0 and 48 hpi
242 by UPLC-nano-ESI-MS/MS as previously described in Herrfurth *et al*. (2020). Phytohormones
243 were extracted with methyl-tert-butyl ether (MTBE), reversed phase-separated using an
244 ACQUITY UPLC® system (Waters Corp., USA) and analysed by nanoelectrospray ionization
245 (nanoESI) (TriVersa Nanomate®; Advion BioSciences, USA) coupled with an AB Sciex 4000

246 QTRAP® tandem mass spectrometer (AB Sciex, USA) employed in scheduled multiple
247 reaction monitoring mode. For quantification, 10 ng D_4-SA (C/D/N Isotopes Inc., Canada),
248 20 ng D_5-IAA (Eurisotop, Germany), and 10 ng D_3-JA-Leu (kindly provided by Otto Miersch,
249 Halle/Saale, Germany) were added at the beginning of the extraction procedure. For detection,
250 the following mass transitions were used: 137/93 (declustering potential (DP) −25 V, entrance
251 potential (EP) -6 V, collision energy (CE) −20 V) for SA, 141/97 (DP −25 V, EP −6 V, CE −22
252 V) for D_4-SA, 179/135 (DP −35 V, EP −9 V, CE -14 V) for D_5-indole-acetic acid, 199/141 (DP
253 −60 V, EP −4 V, CE -32 V) for camalexin, 322/130 (DP −45 V, EP −5 V, CE -28 V) for JA-Ile
254 and 325/133 (DP −65 V, EP −4 V, CE -30 V) for D_3-JA-Leu.
255
256 **2.11 GUS reporter assays**
257 To determine induction of *PR1*, GUS enzyme activity of *PR1::GUS Arabidopsis* plants was
258 determined histochemically on leaves of the reporter line, treated as previously described,
259 collected at 48 hpi, and placed in the GUS staining solution (50 mM sodium phosphate buffer
260 - pH 7, 10mM EDTA, 1 mM $K_3Fe(CN)6$, 2 mM X-GlcA, and 0,1% Triton X-100). The leaves
261 were vacuum-infiltrated for 5 min and incubated for 4 h at 37°C. Next, they were washed with
262 Milli-Q water and left overnight at 4°C in a discoloration / fixation solution (ethanol:acetic acid,
263 3:1). Once the discoloration process was complete, leaves were placed in 95% (v/v) ethanol.
264
265 **2.12 Lipid composition for plant biomimetic membranes**
266 To mimic the lipid composition of plant PM, PLPC, β-sitosterol and GluCer were used, either
267 in a mixture (60:20:20, molar ratio) or alone, depending on the experiment. This lipid
268 composition was previously used to mimic plant PM (Deleu *et al*., 2014, 2019; Deboever *et al*.,
269 2022).
270
271 **2.13 Adsorption of sphinganine onto lipid monolayers using Langmuir trough**
272 Adsorption experiments at constant surface area were performed in a KSV (Helsinki, Finland)
273 Minitrough (190 cm^3) placed on a vibration-isolated table and equipped with a Wilhelmy plate,

274 as previously described (Nasir *et al*., 2016). Lipid solutions were spread at the air-subphase
275 interface to reach the desired initial surface pressure. After a 15 min wait for solvent
276 evaporation and film stabilization, d18:0 was injected in the subphase (10 mM Tris buffer, pH
277 7.4), underneath the pre-formed lipid monolayer to a final concentration of 1.25 µM. The
278 adsorption of d18:0 to the lipid monolayer was monitored by the increase of surface pressure
279 as previously described (Nasir *et al*., 2016; Deleu *et al*., 2019). The injection of ethanol (0.1%)
280 was used as control. The maximal insertion pressure (MIP) and the differential Π_0 ($d\Pi_0$) were
281 determined, indicating the penetration power of d18:0 into the lipid monolayer and the attracting
282 effect the lipids have on d18:0, respectively. The MIP was obtained by linear regression of the
283 plot $\Delta\Pi$ *vs* Π_i and $d\Pi_0$ was calculated as follows: $d\Pi_0 = \Delta\Pi_0 - \Pi_e$
284 $\Delta\Pi_0$ corresponds to the y-intercept of the linear regression of the plot, and Π_e is the surface
285 pressure of d18:0 at the equilibrium when there is no lipid at the interface.
286
287 **2.14 MLVs and liposome preparation**
288 *Multilamellar vesicles*
289 Multilamellar vesicles (MLVs) were prepared as follows, with lipid mixtures of plant lipids. They
290 were dissolved in a chloroform/methanol mix (2:1, v:v). Solvents were evaporated and samples
291 were maintained under vacuum overnight to obtain a dry lipid film. Tris-HCl buffer (10 mM, pH
292 7.4) was then added to hydrate the lipid film. The lipid dispersion was maintained at 37°C for
293 1 h, vortexed every 10 min followed by 5 cycles of freeze-thawing.
294 *Large unilamellar vesicles*
295 To obtain large unilamellar vesicles (LUVs), the MLV suspension was extruded 13 times
296 through a 0,1 µM membrane filter using Liposofast extruder (AVESTIN®). Diameter and
297 stability of the LUVs were confirmed by dynamic light scattering (DLS) measurements.
298
299 **2.15 Thermodynamic parameters of sphinganine interaction with lipid bilayers by**
300 **isothermal titration calorimetry**

301 For isothermal titration calorimetry (ITC) measurements, LUVs were prepared as described
302 and resuspended to reach a final concentration of 1 mM in Tris-HCl buffer (10 mM, pH 7.4). A
303 VP-ITC microcalorimeter (Microcal Inc., Northampton, MA, USA) was used for all
304 measurements. d18:0 was dissolved in DMSO (100%). All experiments were performed at
305 26°C. The reference cell was filled with degassed Milli-Q water. The sample cell (V= 1.4565
306 mL) was filled either with buffer (blank - Tris-HCl, 10 mM, pH 7.4), buffer + d18:0 (at a final
307 concentration of 20 µM) or buffer + DMSO (control – 0,01%). This cell was continuously stirred
308 at 305 rpm. The syringe (V= 300 µL) was filled with the LUV suspension + DMSO (1 mM in
309 buffer + 0.01%). Both the LUV solution and the content of the sample cell were degassed by
310 ultrasonication before use. The first injection of LUVs suspension was 2 µL and was not used
311 in data analysis. Then, every 600 s, 10 µL of the suspension were injected in the sample cell.
312 ITC data were analyzed using Origin 7.0 (Microcal) software following a previously described
313 method (Heerklotz and Seelig, 2000; Lebecque *et al*., 2018).
314
315 **2.16 Laurdan polarization on lipid vesicles LUVs**
316 Liposome suspension at a concentration of 100 µM in lipids was incubated with 1 µM of
317 Laurdan (Sigma-Aldrich) for 1h15. Then, wells of black 96-well microplates (Greiner Bio-
318 One™ CellStar™, Fischer Scientific) were loaded with 100 µL of liposome solution per well.
319 The fluorescence was recorded using Spark® microplate reader (Tecan) with an excitation
320 wavelength at 360 (±35) nm and emission wavelengths at 430 (±20) nm and 485 (±20) nm.
321 The fluorescence was recorded once before treatment and every 5 min until 20 minutes, after
322 the addition of 100 µL of 2-times concentrated treatment.
323 The generalized polarization (GP) was defined as GP = $\frac{(I_{430nm}-I_{485nm})}{(I_{430nm}+I_{485nm})}$, where I_{430nm} and I_{485nm}
324 represents the blank-subtracted fluorescence intensities at emission wavelengths of 430 nm
325 and 485 nm respectively. Variation of GP (ΔGP) is defined as the subtraction of GP measured
326 at each time point following treatment from GP measured before treatment.
327

328 **2.17 Propensity of sphinganine to insert into a bilayer determined by the Impala**
329 **procedure**
330 First, the structure of d18:0 was constructed using HyperChem software (Hypercube, Inc.).
331 The molecular geometry was optimized by systematic analysis of the torsion angles using the
332 structure tree method as previously described (Lins *et al*., 1995). The most probable structure,
333 corresponding to the lowest conformational energy, was used. The Impala procedure uses a
334 Monte Carlo approach to simulate the insertion of d18:0 in an implicit lipid bilayer, as previously
335 described (Ducarme *et al*., 1998; Franche *et al*., 2020). Briefly, this method employs an
336 empirical forcefield to depict membrane physicochemical features while taking into account
337 two types of restraints: the hydrophobic effect and lipid disturbances. The Z axis is assumed
338 to be the only variable in membrane properties. The two restraints were calculated at each
339 place by moving the d18:0 molecules along the Z axis by 1 Å steps from one side of the implicit
340 membrane to the other and were later added to determine the total energy restraint.
341
342 **2.18 Interaction energies between sphinganine and lipids determined by the**
343 **Hypermatrix docking method**
344 The hypermatrix docking method was employed, as previously described (Deleu *et al*., 2014;
345 Deleu *et al*., 2019) in order to dock a molecule of sphinganine to a lipid system composed of
346 either plant or bacterial lipids. Briefly, a molecule of d18:0 is fixed at the center of the system
347 and oriented at the hydrophilic/hydrophobic interface. The lipid molecules, which are also
348 oriented at the interface, are positioned around the center molecule and over 10^7 positions
349 (translations and rotations) are tested. Interactions such as Van der Waals, electrostatic, and
350 hydrophobic are all taken into account when calculating the interaction energies. The energy
351 of interaction along the coordinates of all assembly are gathered in a matrix and sorted
352 according to decreasing values. The assembly with the lowest energy value is considered the
353 energetically most stable.
354

355 **2.19 Modeling of sphinganine/plant lipids monolayer interactions with Big Monolayer**
356 **method**

357 The big monolayer method, as described by Deleu *et al.* (2019), was used to visualize lipid
358 domains. Briefly, the initial stage consisted in aligning each pair of molecules in the system at
359 the hydrophilic/hydrophobic interface according to Hypermatrix. Then, their interaction
360 energies were computed, considering Van der Waals, electrostatic, and hydrophobic
361 interactions. The second phase involved creating a grid of 200 × 200 molecules and utilizing a
362 Monte Carlo procedure to minimize the system using the interaction energies computed in the
363 previous step. Each molecule is represented by a pixel, producing an image of the molecular
364 domains formed. Three repetitions of the system were calculated. The simulations were
365 performed using plant lipid mixture with or without d18:0 (88% lipids, 12% d18:0).
366

367 **2.20 Protoplast isolation**

368 The isolation of mesophyll protoplasts was carried out by an enzymatic method as previously
369 described (Yoo *et al*., 2007). Briefly, leaves of *Arabidopsis* were harvested, their abaxial side
370 abraded with a scalpel blade and placed abaxial face down in an enzymatic solution (20 mM
371 MES, 400 mM mannitol, 20 mM KCl, 10 mM $CaCl_2$, 1.5% cellulase, 0.4% maceroenzyme).
372 They were left overnight at room temperature in the dark in this solution. The next day the
373 digested solution was filtered with a gauze and centrifuged at 300 g for 2 min. The supernatant
374 was removed, and a rinsing solution was added (20 mM MES, 400 mM mannitol, 20 mM KCl,
375 10 mM $CaCl_2$). This operation was repeated two times. The last supernatant was discarded,
376 and the protoplasts were resuspended at 10^6 protoplasts/mL in a storage solution (20 mM
377 MES, 400 mM mannitol, 20 mM KCl, 10 mM $CaCl_2$) until further use.
378

379 **2.21 Atomic force microscopy**

380 Protoplasts were adhered to the bottom of a glass-bottom Petrie dish by coating with positive-
381 charge-bearing protamine sulphate 1 % in water: the bottom of the Petri dish was covered with
382 a thin layer of this solution during 2 min, rinsed 3 times with the protoplasts storage solution

383 and the remaining solution was discarded. Protoplast suspension was incubated for 5 min with
384 final concentration 2 µM or 5 µM of d18:0 or control ethanol in protoplasts storage solution for
385 5 min. Then, pre-treated or not protoplasts suspension was gently deposited to the coating
386 Petri Dish, and the protoplasts were settled for 5 min.
387 QNM-LC-CAL probes (Bruker, Billerica, USA), having a resonance frequency of 45 kHz, a tip
388 radius of 65 nm, a tip height of 16 µm and a nominal spring constant below 100 mN/m were
389 calibrated on a non-compliant sample to extract the deflection sensitivity which turned out to
390 be around 10 nm/V. Afterwards the tip was pulled off (of 100 Um) and tuned in liquid to
391 determine the spring constant.
392 Optics (Nikon Ti 2000, Nikon, Tokyo, Japan) were used in bright field mode to browse through
393 all protoplasts and focus on those having a 100 µm diameter. Therefore, the tip was engaged
394 at the very center of each and forces curves were captured in single force spectroscopy mode.
395 The atomic force microscopy (AFM) used was a Bioscope Catalyst (Bruker, Billerica, USA). A
396 z ramp output was used, with a ramp size of 5 µm, a ramp rate of 0.25 Hz, a contact time of
397 50 msec, and a forward and backward velocities of 5 µm/sec. Each force curves contained
398 2048 points. The Poisson's ratio was arbitrary set at 0.3. We used a relative trigger mode, a
399 tip threshold of 30 nm and plotted the deflection error as data type. It was verified that there
400 was no apparent change in diameter or x,y motion of the object during the acquisition.
401 The Young's modulus was extracted according to the Hert's theory and normalized as a
402 function of the protoplasts' volumes. A minimum of 50 curves per condition were recorded and
403 experiments were repeated three times.
404
405 **2.22 Confocal microscopy**
406 To determine the membrane order, protoplasts were labelled with 300 nM final concentration
407 of fluorescent probe di-4-ANEPPDHQ (Invitrogen, D36802, stock solution 1,5 mM in DMSO)
408 in protoplast storage solution, during 5 min. The labelled protoplasts suspension was gently
409 deposited to the bottom of a glass bottom Petri dish and the protoplasts were settled for 5 min.

410 The labelled protoplast suspension was incubated for 5 min with final concentration 2 µM or 5
411 µM of d18:0 or control ethanol for 5 min.
412 Fluorescence images were acquired using a laser scanning microscope LSM 880 from ZEISS
413 (Carl ZEISS SAS, Rueil Malmaison, France) through 63x (ON 1,4) oil immersion objective with
414 ZEN software. Di-4-ANEPPDHQ excitation was done at 488 nm and emission intensities were
415 acquired between 540–560 nm (green image) and between 630–650 nm (red image).
416 Ratiometric imaging was performed using the Fiji software (Schindelin et al., 2021) with a
417 dedicated home-made macro.
418

419 **3. Results**

420 **3.1 Effect of *Pst AvrRpm1* and sphinganine co-infiltration on *Arabidospis* cell**
421 **death**

422 We and others previously demonstrated that the co-infiltration of *Pst AvrRpm1* and
423 d18:0 or t18:0, respectively, does not induce an HR in contrast to what happens with
424 an infiltration of an avirulent bacteria or LCB alone (Magnin-Robert *et al.*, 2015; Glenz
425 *et al*., 2022). Therefore, *Pst* expressing effectors other than AvrRpm1 were selected to
426 elucidate whether the absence of visible HR was dependent on the effector. AvrRpt2
427 was chosen because, like AvrRpm1, it is associated to the PM with RIN4 (Boyes *et al*.,
428 1998; Mackey *et al*., 2003; Xin *et al*., 2018). AvrRps4 was also tested because of the
429 cytoplasmic localization of its target, RPS4 (Gassmann *et al*., 1999; Wirthmueller *et al*.,
430 2007).

431 As expected, treatment with *Pst* DC3000 co-infiltrated or not with d18:0 triggered
432 typical disease symptoms and infection with *Pst AvrRpm1*, *Pst AvrRpt2* or *Pst AvrRps4*
433 alone, gave rise to a typical HR. Whereas co-infiltration of *Pst AvrRpm1* and d18:0 did
434 not induce a visible HR as expected, the other tested bacteria displayed an HR when
435 co-infiltrated with the sphingolipid (Figure 1A). Changes in conductivity were then used
436 as a marker of plant cell death, as PM damages result in strong electrolyte leakage
437 (Kawasaki *et al*., 2005) (Figure 1B). All treatments triggered an increase in conductivity
438 between 4 and 24 hpi, except for co-infiltration with *Pst AvrRpm1* and d18:0, displaying
439 a conductivity stable over time and similar to the control plants (Figure 1B). These
440 findings are consistent with our previous study (Magnin-Robert *et al*., 2015) and
441 corroborated with phenotypic observations in Figure 1A.

442

443 **3.2 *In vitro* and *in planta* growth of *Pst AvrRpm1* in presence of sphinganine**

444 As a potential deleterious effect of d18:0 on the bacteria could not be excluded, *in vitro*
445 bacterial growth measurements were undertaken with or without the sphingolipid in the
446 culture medium (Figure 2A). Ethanol had no effect on bacterial growth of all tested
447 strains (data not shown). Interestingly, d18:0 had no antibacterial effect on *Pst*
448 *AvrRpm1* and out of all the bacteria tested, d18:0 slightly reduced the growth rate of
449 *Pst AvrRpt2*. Surprisingly, this bacterium does provoke cell death when co-infiltrated
450 into leaves.
451 To determine the effect of the co-infiltration on bacterial growth *in planta*, bacterial
452 populations were quantified at 0 and 48 hpi (Figure 2B). The growth of the avirulent
453 strain *Pst AvrRpm1* was slightly reduced compared to the virulent strain, *Pst* DC3000
454 at 48 hpi. Furthermore, while the co-infiltration had no consequence on the
455 development of *Pst* DC3000, it slightly reduced *Pst AvrRpm1* growth at 48 hpi. This
456 bacterial count was however two-fold higher at 48 hpi than at 0 hpi, like in the other
457 conditions (Figure 2B). Collectively, these data suggest that d18:0 does not have an
458 antibacterial effect that could explain the absence of HR when *Pst AvrRpm1* is co-
459 infiltrated with d18:0. Moreover, while *Pst AvrRpm1* continues its development inside
460 the plant, it is however incapable of triggering an HR.
461
462 **3.3 Extracellular ROS production by *Arabidopsis* in response to infection by *Pst***
463 Strong and sustained extracellular ROS production is an early defense event generally
464 linked to HR. We therefore monitored their production by *Arabidopsis* in response to
465 *Pst AvrRpm1*, *Pst AvrRpt2* and *Pst AvrRps4* (Figure 3). No significant statistical
466 difference was found between ROS production triggered by bacteria alone or mixed
467 with ethanol (data not shown). As already observed by Magnin-Robert *et al.* (2015),
468 co-treatment of *Pst AvrRpm1* but also of *Pst AvrRpt2* and *Pst AvrRps4* with d18:0

469 reduced extracellular ROS production by approximatively 6-, 2- and 1.7-fold,
470 respectively (Figure 3). Only the co-infiltration of *Pst AvrRpm1* and d18:0 did not result
471 in an HR but ROS levels appear to be dramatically affected even with other bacteria
472 like *Pst AvrRps4*. These results suggest that reduced ROS production is not directly
473 linked to the absence of HR.
474
475 **3.4 Effects of *Pst AvrRpm1* and sphinganine co-infiltration on *Arabidopsis* late**
476 **defense responses**
477 Considering the effects of d18:0 on ROS production and cell death development, other
478 markers of plant defense were studied in response to co-infiltration. The accumulation
479 of the phytoalexin camalexin as well as the hormones SA and JA-Ile was followed. The
480 expression of *PATHOGENESIS-RELATED GENE 1* (*PR1*) and *VEGETATIVE*
481 *STORAGE PROTEIN 1* (*VSP1*), marker genes of SA and JA-Ile signaling pathways,
482 respectively, was also analyzed. Control infiltration did not induce camalexin
483 production (Figure 4A). At 48 hpi, *Pst* DC3000 inoculation with or without d18:0
484 triggered similar camalexin accumulation. However, d18:0 co-infiltration did
485 significantly reduce camalexin production in response to *Pst AvrRpm1* since it
486 decreased from ~250 nmol/g FW to a similar level observed in controls (~3 nmol/g FW)
487 at 48 hpi (Figure 4A). Overexpression of *PR1* was observed 48h after infiltration with
488 each *Pst* strain alone (Figure 4C), which correlated with the accumulation of SA (Figure
489 4E). Neither SA accumulation nor *PR1* expression was induced at earlier time points.
490 The use of an *Arabidopsis* reporter line *PR1::GUS* confirmed the induction of *PR1*
491 expression in treated leaves (Figure 4B). Both SA accumulation and *PR1*
492 overexpression are repressed when leaves are co-infiltrated with d18:0, leading to
493 similar levels as in control plants (Figure 4C and E). *VSP1* is weakly expressed in

494 response to *Pst* DC3000 but overexpressed when this bacterium is co-infiltrated with
495 d18:0 (~ 9-fold and ~ 6-fold more at 6 and 48 hpi, respectively) (Figure 4D). JA-Ile
496 levels are however higher with the bacterium alone than co-infiltrated (Figure 4F).
497 When *Arabidopsis* was inoculated with *Pst AvrRpm1*, *VSP1* was slightly
498 overexpressed at 48 hpi but repressed when co-infiltrated with d18:0 (Figure 4D). JA-
499 Ile levels were concomitantly low (Figure 4F), as expected from plants challenged with
500 avirulent *P. syringae* (Mur *et al.*, 2006). Overall, co-infiltration of *Pst AvrRpm1* with
501 d18:0 significantly lowers the amount of camalexin and both defense hormone
502 signaling pathways.
503
504 **3.5 Involvement of RPM1 and RIN4 in the absence of HR**
505 Once injected into the cytoplasm of the host, AvrRpm1 triggers the phosphorylation of
506 RIN4, inducing the activation of RPM1 and subsequently the ETI leading to an HR
507 (Nimchuck *et al.*, 2000). To elucidate whether RPM1 and / or RIN4 were involved when
508 the bacterium is co-infiltrated with d18:0, inoculations of *Pst AvrRpm1* were performed
509 on *Arabidopsis* mutants *rpm1-3,* and *rpm1-rps2-rin4,* as well as the complemented line
510 *RPM1-myc rpm1*. Infiltration of the bacteria alone induced cell death and co-infiltration
511 of the complemented line displayed no symptoms, as expected (Figure 5A). Despite
512 lacking RPM1 and / or RIN4, all mutants showed the same phenotype as the WT when
513 co-infiltrated with d18:0 as they did not exhibit visible cell death (Figure 5A). It has been
514 previously demonstrated that RPM1 is degraded during the first hpi, coincidently with
515 the onset of the HR (Boyes *et al.*, 1998). To further elucidate the role of RPM1 and
516 RIN4, *RPM1-myc rpm1* plant was used to monitor the degradation of RPM1 following
517 inoculation (Figure 5B). Western blot analysis showed that while RPM1 was degraded
518 around 4 to 6 hpi when *Pst AvrRpm1* was infiltrated alone, the protein was still detected

519 24 hpi when the bacteria was co-infiltrated (Figure 5B). Taken collectively, these data
520 suggest that the mechanism underlying the absence of HR occurs upstream of RPM1
521 degradation.
522
523 **3.6 Effect of *Pst AvrB* and *Pst AvrPphB* co-infiltration with sphinganine on**
524 ***Arabidopsis* defense response**
525 The three effectors AvrRpm1, AvrB and AvrPphB share an eukaryotic *N*-myristoylation
526 site in their protein sequences that allows them to be redirected to the PM once they
527 have entered their host (Nimchuk *et al*., 2000). Like AvrRpm1, AvrB interacts with
528 RPM1 and RIN4 (Grant *et al*., 1995; Lee *et al*., 2004), and AvrPphB with RPS5 and
529 PBS1, both located at the PM (Ade *et al*., 2007; Pottinger and Innes, 2020). As already
530 demonstrated (Warren *et al*., 1998; Whalen *et al*., 1991), infiltration of *Pst AvrB* or *Pst*
531 *AvrPphB* triggers an HR. No cell death was visible when both *Pst AvrB* and *Pst*
532 *AvrPphB* were co-infiltrated with d18:0, suggesting HR was not triggered in treated
533 plants, similarly to *Pst AvrRpm1* (Figure 6A). Further tests were conducted to
534 determine if d18:0 had an *in vitro* effect on these bacteria. Their growth rate remained
535 unchanged after d18:0 addition (Figure 6B), confirming that d18:0 has no antibacterial
536 effect on these two bacteria. Extracellular ROS production by *Arabidopsis* in response
537 to *Pst AvrB* and *Pst AvrPphB* was also monitored (Figure 6C). As for *Pst AvrRpm1*,
538 d18:0 significantly reduced this production in response to both bacteria (~ 2-fold for *Pst*
539 *AvrB* and ~ 3-fold for *Pst AvrPphB*).
540
541 **3.7 *NMT1* relative expression following *Pst AvrRpm1* and sphinganine co-**
542 **infiltration**

543 In *Arabidopsis*, two enzymes, NMT1 and NMT2, are responsible for *N*-myristoylation
544 (Pierre et al., 2007). As the corresponding mutants displaying severe phenotypes, they
545 were thus not suitable for our experiments. We used qRT-PCR to determine
546 expression patterns of *NMT1* and *NMT2* in response to infiltration of *Arabidopsis* WT
547 leaves with *Pst* DC3000 or *Pst AvrRpm1*, either alone or with d18:0 (Figure 7).
548 Unfortunately, the expression of *NMT2* was too low to be detectable. At 6 and 24 hpi,
549 *NMT1* expression in plants infiltrated with *Pst* DC3000 alone or with d18:0 was similar
550 to that of control samples but was induced at 48 hpi (~ 2-fold). When plants were
551 infiltrated with *Pst AvrRpm1* alone, a continuous stimulation of *NMT1* expression is
552 observed during the time-course experiment to reach a ~2.2-fold induction at 48 hpi
553 (Figure 7). However, when plants were co-infiltrated with *Pst AvrRpm1* and d18:0, no
554 induction could be observed during the time-course experiment (Figure 7). Thus, a
555 decrease of ~1.7-fold is observed between *Pst AvrRpm1* infiltrated alone and with
556 d18:0. Overall, these results suggest that co-infiltration with d18:0 modifies *NMT1*
557 expression in response to infection with *Pst AvrRpm1*.
558

559 **3.8 Interaction capacity of sphinganine with plant plasma membrane-mimicking**
560 **models**

561 It has been shown that LCB sphingosine (d18:1) can increase the permeability of
562 liposomal and erythrocyte ghost membranes to aqueous solutes (Contreras *et al*.,
563 2006). Based on this finding, d18:0 was hypothesized to interact with the lipids of plant
564 PM. To investigate this hypothesis, we conducted *in silico* and *in vitro* biophysical
565 analyses using membrane plant models. Thanks to their defined structure and
566 controlled lipid composition, these models were found to be useful in understanding

567 how external molecules affect the organization and mechanical properties of the
568 membranes (Deleu *et al*., 2014; Furlan *et al.*, 2020; Cordelier *et al*., 2022).

569 The Impala modeling method was used to predict the ability of d18:0 to insert into an
570 implicit model lipid bilayer and to determine the preferable location and positioning of
571 d18:0 within a membrane bilayer (Figure 8). The more negative the energy is, the more
572 favorable the insertion will be. A sharp drop of energy was observed as d18:0 moved
573 from the aqueous phase to the membrane surface (up to ~-10 Kcal/mol), indicating that
574 it could easily insert into membranes. The energy was close to 0 Kcal/mol in the
575 hydrophobic region of the membrane, suggesting that d18:0 has a less favorable
576 interaction with this region compared with the lipid bilayer hydrophilic region (Figure
577 8A). Nevertheless, the non-positive energy value in the hydrophobic region of the
578 bilayer suggests that d18:0 could flip-flop between the two bilayer leaflets. A large
579 increase in energy (from ~-10 Kcal/mol to +6.7 Kcal/mol) is also observed when d18:0
580 moves from the inner bilayer leaflet to the aqueous medium, which strongly suggests
581 that d18:0 has no propensity to cross the membrane and enter into the cytoplasm. The
582 preferred positioning of d18:0 within the membrane is shown in Figure 8B. Its lipid chain
583 lies within the hydrophobic part of the membrane while the amine and alcohol groups
584 are located in the hydrophilic part of the bilayer. Altogether, this indicates that d18:0
585 can interact with membranes and remains there. To support these simulation results,
586 experimental analyses were performed using large unilamellar vesicles (LUVs) that
587 mimic plant PM, consisting of palmitoyl-2-linoleoyl-*sn*-glycero-3-phosphocholine
588 (PLPC), glucosylceramide (GluCer) and β-sitosterol (sito) as the plant PM model
589 phospholipid, sphingolipid and sterol respectively (Deleu *et al*., 2014; Rondelli *et al*.,
590 2021; Deboever *et al*., 2022).

591 Results from ITC experiments showed a negative and decreasing heat flow after each
592 LUV injection into the d18:0 solution (Figure 9A), indicating that d18:0 interacts with
593 plant PM-mimicking LUVs. The thermodynamic parameters calculated from the fitting
594 of raw data are presented in Figure 9B. The binding coefficient K was relatively high
595 (>80 mM^{-1}) suggesting that d18:0 has a strong affinity for plant-mimicking lipid
596 membranes confirming the low probability that it emerges in the intracellular medium.
597 This affinity for plant PM-like liposomes is higher than that observed for other plant-
598 eliciting molecules such as linoleic and linolenic acid hydroperoxides (<3 mM^{-1}; Deleu
599 *et al*., 2019), and rhamnolipid bolaforms (7.5 mM^{-1}; Luzuriaga-Loaiza *et al*., 2018). The
600 binding reaction of d18:0 to LUVs was spontaneous as the molar free energy ΔG was
601 negative, exothermic as the molar enthalpy change ΔH was negative and generated a
602 positive change of the molar entropy (TΔS>0). The higher absolute value of the molar
603 entropy (TΔS>0) compared to the absolute value of the molar enthalpy change (ΔH),
604 indicates that the interactions is entropy-driven, i.e. mostly of hydrophobic nature.
605 Altogether, these results suggest that d18:0 is attracted by and can interact with plant
606 lipid membranes.
607

608 **3.9 Lipid specificity of the interaction between sphinganine and plant plasma**
609 **membrane-mimicking models**

610 To investigate specific interactions between d18:0 and lipids representative of plant
611 PM, the Langmuir trough technique was used to analyze the adsorption capacity of
612 d18:0 into monolayers of each individual lipid. In this technique, a lipid monolayer is
613 initially formed at an air-water interface, and then d18:0 is injected into the subphase
614 beneath the monolayer. The increase in surface pressure (ΔΠ) at a constant trough
615 area was monitored to determine the adsorption of d18:0 into the lipid monolayer at

616 different initial surface pressures (Π_i) (Figure S1). Two parameters were determined
617 from these data (Figure 10A): (i) the differential surface pressure ($d\Pi_0$), which provides
618 information on the attractive effect of the lipids on d18:0, and (ii) the maximal insertion
619 pressure (MIP), which reflects the ability of d18:0 to penetrate into the lipid monolayer
620 (Deleu et al., 2014). Upon insertion of d18:0 onto monolayers formed with individual
621 plant PM lipids, $d\Pi_0$ values were all positive and similar for all compositions, indicating
622 that all tested lipids exert a similar attraction on d18:0 (Figure 10A). MIP values were
623 all higher than the lateral pressure supposed to prevail into biological membranes (30
624 – 35 mN/m) (Marsh, 1996), meaning that d18:0 may be able to adsorb into natural plant
625 membranes.

626 Lipid specificity of the interaction was also studied by an *in silico* approach using the
627 Hypermatrix docking method. This method calculates the energy of interaction
628 between d18:0 and individual plant lipids at a hydrophilic/hydrophobic interface,
629 indicating whether this interaction is energetically favorable or not (Brasseur *et al*.,
630 1987; Deleu *et al*., 2014). Results showed that the interaction between d18:0 and all
631 plant lipids was favorable as all interaction energies are negative (Figure 10B).
632 Interestingly, the interaction energies between d18:0 and plant lipids were more
633 favorable than those observed for d18:0 with itself. With this method, interaction
634 between d18:0 and PLPC or GluCer appeared to be more favorable than with β-
635 sitosterol.

636 Altogether, these data showed that d18:0 is attracted by and could interact with lipids
637 of plants. There is however no clear trend to determine a preferential interaction of
638 d18:0 with a particular lipid.
639

640 **3.10 Modification of the organization and mechanical properties of plant plasma**
641 **membrane-mimicking models induced by sphinganine**

642 Since d18:0 can interact with lipids found in plant PMs, additional experiments were
643 conducted to investigate how these interactions could impact the mechanical
644 properties and the organization of plant PMs.
645 Two aspects of membrane mechanics were considered: membrane fluidity and
646 membrane elasticity. Membrane fluidity refers to the degree of lipid packing and the
647 mobility or dynamics of lipids within the membrane, which can be characterized by the
648 order level parameter (Gerbeau-Pissot *et al*., 2014). Membrane elasticity
649 corresponding to the resistance of a material to deformation when subjected to an
650 applied force was determined by measuring the Young's modulus. The higher the
651 Young's modulus, the stiffer and less deformable the object is (Magazzu and
652 Marcuello, 2023). Although membrane fluidity can be influenced by the membrane
653 elasticity, there is no direct quantitative relationship between Young's modulus and
654 membrane fluidity or order level and therefore must be considered as separate aspects
655 of membrane behavior.
656 To analyze the order level of *Arabidopsis* PM in response to d18:0, *Arabidopsis* leaf
657 protoplasts were stained with the dye di-4-ANEPPDHQ. The order level of the
658 membrane, revealed by fluorescence imaging, was quantified using the red/green ratio
659 of the membrane (RGM) (Dinic *et al*., 2011; Gerbeau-Pissot *et al*., 2014). Observations
660 of protoplasts indicated a significant decrease in RGM compared to controls (from 0.99
661 to 0.80 and 0.74 for concentrations of 2 µM and 5 µM d18:0, respectively) (Figure 11A-
662 D), with no statistical difference between the two concentrations of d18:0. The RGM
663 profile of a 4 µm fragment of PM from controls appeared homogenous whereas those
664 from sphingolipid-treated protoplasts is more heterogenous (Figure 11E-G). These

665 findings suggest that the order level increased in response to the LCB. This increase
666 in membrane order level in the presence of d18:0 was confirmed by the greater
667 variation in the generalized polarization of Laurdan on biomimetic liposomes compared
668 to the control ethanol, and this as soon as d18:0 came in contact with the lipid bilayer
669 (Figure 11H). Laurdan is a fluorescent probe sensitive to membrane lateral packing, a
670 higher generalized polarization corresponding to a greater lipid packing (Parasassi *et*
671 *al*., 1991).

672 Young's modulus was measured by recording force-distance curves using AFM (Supp
673 data) on leaf protoplasts. In the presence of d18:0, Young's modulus decreased (Figure
674 11I) indicating a reduction in membrane elasticity and a lower resistance to membrane
675 deformation. Again, there is no concentration dependence.

676 Using the Big Monolayer simulation method, which is useful for studying the lateral
677 distribution of molecules based on their mutual interaction energies, we observed that
678 d18:0 preferentially interacted with the lipid domains initially formed by β-sitosterol and
679 GluCer (Figure 11J left), resulting in their fragmentation as shown in Figure 11J right.
680 Accordingly, fluorescence images of di-4-ANEPPDHQ-stained protoplasts (Figure 11
681 A to C and E to G) demonstrated an increase in the number of small ordered domains
682 in the presence of d18:0 compared to its absence.
683
684

685 **4. Discussion**

686 The roles of sphingolipids during PCD in response to biotic stress are still not fully
687 understood (Berkey *et al*., 2012; Huby *et al*., 2020). Previous studies showed that co-
688 infiltration of *Pst AvrRpm1* with the LCB d18:0 or t18:0 on *Arabidopsis* leaves did not
689 trigger an HR on the treated leaves, with no evidence of cell death, indicating the
690 conservation of plant PM integrity and absence of cell lysis following the co-infiltration
691 (Glenz *et al*., 2022; Magnin-Robert *et al*., 2015). In the present work, we show that the
692 levels of all plant immunity markers in response to co-infiltration, including those related
693 to the plasma membrane, are similar to the control plants, despite the fact that the
694 bacterium still develops inside plant tissues. We also report a similar effect with *Pst*
695 expressing the effector AvrB or AvrPphB. AvrRpm1, AvrB and AvrPphB need to be
696 myristoylated to be active. This process is disturbed during co-infiltration leading to an
697 absence of plant defense response activation. Finally, interaction of d18:0 with lipids
698 of the plant PM was demonstrated.

699 *In vitro* tests showed that this LCB does not have an antibacterial effect on *Pst*
700 *AvrRpm1*, *Pst AvrB* and *Pst AvrPphB*, similarly to results obtained with *P. aeruginosa*
701 (Fischer *et al*., 2012). t18:0 was shown to inhibit *Pst* growth (Glenz *et al*., 2022).
702 However, the authors used a smaller bacterial concentration and LB medium to
703 perform their tests. Here, by using a higher bacterial concentration and a medium more
704 favorable to *Pst* growth, the bacterial pressure was more important in our tests, which
705 could explain the discrepancy with the data published by Glenz and colleagues. *In*
706 *planta* experiments showed that, even though *Pst AvrRpm1* is not capable of inducing
707 an HR when co-infiltrated with d18:0, it is still present inside the plant and even
708 continues to thrive, confirming the non-detrimental effect of d18:0 on the bacterium. In
709 contrast, a pre-treatment with FB1, in order to promote endogenous LCB accumulation,

710 inhibit *Pst* DC3000 but not *Pst AvrRpm1* growth (Saucedo-García *et al*., 2023).
711 Moreover, *loh1* plants that accumulate endogenous levels of LCBs together with *PR1*
712 enhanced expression, displays spontaneous cell death (Ternes *et al*., 2011). The
713 localization (apoplastic *vs* cytoplasmic) of the LCB and the fact that FB1 or *loh1* induces
714 or displays higher LCB but also LCB-P, ceramide or GluCer accumulation (Chen *et al*.,
715 2008; Kimberlin *et al*., 2016; Saucedo-García *et al*., 2011) could explain this
716 discrepancy. This could also suggest that interaction of d18:0 with the PM and its
717 presence within the PM when infiltrated could be essential in the cell death induction.
718 Previous results showed that co-treatment of d18:0 with *Pst* DC3000 or with *Pst*
719 *AvrRpm1* drastically reduced extracellular ROS production by *Arabidopsis* (Magnin-
720 Robert *et al*., 2015). Our results demonstrate that d18:0 reduces ROS production in
721 response to bacteria that induce symptoms *in planta* but also to bacteria that do not
722 induce symptoms (*Pst AvrRps4* and *Pst AvrRpm1, Pst AvrB, Pst AvrPphB,*
723 respectively). This production remained unchanged when plants are treated with *Pst*
724 *AvrRpt2*. The hypothesis that LCBs could impact ROS production by plants has already
725 been put forward in several studies, although some of them are somewhat
726 contradictory. Coursol *et al*. (2015) showed that exogenous addition of 20 µM LCBs
727 reduced tobacco ROS production in response to cryptogein. In *Arabidopsis*, LCBs can
728 induce both intracellular as well as extracellular ROS production (Glenz *et al*., 2019;
729 Peer *et al*., 2011; Shi *et al*., 2007; Saucedo-Garcia *et al*., 2023). ROS production can
730 be detected during both PTI and ETI (Torres, 2010). In *Arabidopsis,* it is mainly related
731 to RbohD located in lipid microdomains of the plant PM (Hao *et al*., 2014; Mongrand *et*
732 *al*., 2004). A number of studies have suggested that RbohD-derived ROS production
733 is not directly involved in plant cell death, but rather in the signaling pathways
734 associated with plant defense responses (Lherminier *et al*., 2009; Torres *et al*., 2005).

735 This means that even though d18:0 could alter ROS production, it may not have any
736 impact on PCD and would therefore not be responsible for the absence of HR.
737 Additionally, it has been already demonstrated that a lipidic elicitor is able to interact
738 with lipid membrane microdomains (Rossard *et al*., 2010). These data suggest that
739 LCBs might interact with and thus disturb the PM organization of *Arabidopsis* leading
740 to the reduction of RbohD activity.
741 SA pathway is triggered in response to hemibiotrophic pathogens, such as *Pst*,
742 whereas JA and its active form JA-Ile are involved in infection by necrotrophic
743 pathogens (Li *et al*., 2019). In our study, *PR1* is significantly down-regulated upon co-
744 infiltration with d18:0 and *Pst* DC3000, and even more so upon *Pst AvrRpm1,* which
745 coincides with lower SA accumulation. SA repression is commonly associated with
746 promotion of bacterial development and/or enhancement of a JA-dependent pathway
747 (Brooks *et al*., 2005; Moore *et al*., 1989; Zhou *et al*., 1998). *P. syringae* produces
748 coronatine, a phytotoxin that mimics JA-Ile and acts by inhibiting the accumulation of
749 SA in order to promote bacterial growth (Zheng *et al*., 2012). Conversely, in
750 *Arabidopsis*, coronatine-insensitive mutants that are resistant to *Pst* display higher
751 levels of SA (Block *et al*., 2005). In *Arabidopsis*, the SA and JA pathways antagonize
752 each other (Li *et al*., 2019; Mur *et al*., 2006). However, JA pathway markers are also
753 down-regulated in response to d18:0/*Pst AvrRpm1* infiltration. Considering these
754 results, we could conceive that co-infiltration represses or does not activate both SA
755 and JA pathways in response to the avirulent bacterium because of a lowered bacterial
756 virulence, a decreased susceptibility, and/or an altered perception of the pathogen.
757 AvrRpm1, AvrB, and AvrPphB effectors all possess a consensus N-terminal
758 myristoylation sites which are required for full avirulence function (Nimchuk *et al*.,
759 2000). Myristoylation process occurs inside the plant cell (Nimchuk *et al*., 2000) and is

760 catalyzed by NMT (*N*-myristoyltransferase) enzymes (Pierre et al., 2007). Here, *NMT1*
761 expression is significantly reduced at 24 and 48 hpi when *Pst* AvrRpm1 is co-infiltrated
762 with d18:0. d18:0 co-infiltration could thus interfere with the myristoylation of these
763 effectors. As a consequence, it prevents them from being redirected to the PM where
764 their targets are and consequently preventing their activity in *Arabidopsis*. Recently, a
765 mis-localization of RPM1 at the PM, due to a depletion in anionic phospholipids in the
766 PM, inhibits its cell death activity (Saile et al., 2021). Since cell death is still induced,
767 such depletion does not affect RPS5 function, which is constitutively PM localized due
768 to the presence of myristoylation motifs in its sequence. RPS5 mediates the recognition
769 of AvrPphB. Co-infiltration of this effector with d18:0 results in an absence of HR, thus
770 excluding the involvement of a PM phospholipid dependent mechanism. PM
771 localization and stability of NLRs is essential for their activity in the induction of cell
772 death and immune responses (Saile et al., 2021). Effector localization into plant cell is
773 also essential for their interaction with their targets and subsequent activity (Nimchuk
774 et al., 2000). The inability for AvrRPM1 to interact with its target implies not only that
775 all the downstream plant defense responses are not activated but also the absence of
776 RPM1 degradation after co-infiltration. Moreover, mutation of consensus myristoylation
777 sites of *AvrRPM1* or *AvrB* leads to a highly reduction of HR events and an unhindered
778 pathogen growth (Nimchuk et al., 2000), consistent with our results.
779 All the effects of d18:0 previously mentioned, and its amphiphilic nature suggest that
780 the molecule can interact with the plant PM. It was thus hypothesized that it could insert
781 into the lipid fraction of the PM, as already suggested for other molecules such as fatty
782 acid hydroperoxides, rhamnolipids, lipopeptides that interact with lipids of plant PMs
783 (Cordelier et al., 2022; Deboever *et al*., 2022; Deleu *et al*., 2013, 2008; Henry *et al*.,
784 2011; Nasir *et al*., 2010; Schellenberger et al., 2021). Here, biophysical studies have

785 shown that d18:0 was attracted by, interacted with and stayed in biomimetic plant PMs.
786 These findings were further supported by *in silico* and *in vitro* analyses as well as
787 microscopic observations that notably showed d18:0 could disturb the lateral
788 organization and mechanical properties of plant PM and more specifically of its
789 microdomains. While it was suggested that exogenous LCB could cross the PM by
790 passive diffusion (Glenz *et al*., 2019), our results suggested that d18:0 has no
791 propensity to go into the intracellular medium but actually possesses a flip-flop potential
792 within the PM meaning that exogenous addition of d18:0 could disturb the PM. As
793 previously stated, this interaction could eventually disturb defense-related proteins
794 located within its domains (Gronnier *et al*., 2018, 2016; Huby *et al*., 2020; Mamode
795 Cassim *et al*., 2019; Nagano *et al*., 2016), which could explain the absence of
796 extracellular ROS production observed in response to *Pst*. Lipid composition and
797 organization of the PM influence PM localization and stability of NLRs and
798 consequently their activity in cell death inducing (Saile et al., 2021). By disturbing the
799 PM organization, exogenous addition of d18:0 could also influence NLR localization
800 and function.
801 Collectively, our results demonstrated that d18:0 could have a dual effect on the PM
802 when co-infiltrated with *Pst AvrRpm1* by disturbing the organization and mechanical
803 properties of the PM and the myristoylation process, and thus the redirection of
804 effectors to the PM. Both actions prevent the interactions of NLR with its effector and
805 subsequent defense responses.
806

807 **Acknowledgement**

808 The authors thank Prof. Jeff Dangl (University of North Carolina, USA), Dr. Farid El-Kasmi
809 (University of Tübingen, Germany), Prof. Brian Staskawicz (University of California, USA),
810 Prof. Jane Parker (Max-Planck Institute, Cologne, Germany) and Dr. Brad Day (Michigan State
811 university, USA) for generously providing the different bacterial strains used in this study.

This work was supported by the National Fund for Scientific Research (FNRS, Belgium), the SFR Condorcet (18ARC107), and the "Fondation Universitaire de Belgique" (Belgian University Foundation). GG was supported by the Foundation for Training in Industrial and Agricultural Research (FRIA, FNRS, grant 1.E.069.20F), and MD is Senior Research Associates of the FNRS. I.F. acknowledges funding by the Deutsche Forschungsgemeinschaft (INST 186/822-1).

Conflict of interest statement

The authors declare no conflict of interest.

Data availability statement

The data that support the findings of this study are available from the corresponding author upon reasonable request.

Orcid

Sylvain Cordelier: https://orcid.org/0000-0001-7723-4145
Jérôme Crouzet: https://orcid.org/0000-0003-0458-830X
Magali Deleu: https://orcid.org/0000-0001-8255-2965
Sandrine Dhondt-Cordelier: https://orcid.org/0000-0002-3778-6727
Stéphan Dorey: https://orcid.org/0000-0002-9583-2824
Ivo Feussner: https://orcid.org/0000-0002-9888-7003
Florence Fontaine: https://orcid.org/ 0000-0003-2918-8812
Guillaume Gilliard: https://orcid.org/0000-0002-4651-2920
Cornelia Herrfurth: https://orcid.org/0000-0001-8255-3255
Cédric Jacquard: https//orcid.org/0000-0003-4284-6082

References

Ade, J., DeYoung, B.J., Golstein, C., Innes, R.W., 2007. Indirect activation of a plant nucleotide binding site-leucine-rich repeat protein by a bacterial protease. Proceedings of the National Academy of Sciences U.S.A. 104, 2531–2536.

Ali, U., Li, H., Wang, X., Guo, L., 2018. Emerging roles of sphingolipid signaling in plant response to biotic and abiotic stresses. Molecular Plant 11, 1328–1343.

Bari, R., Jones, J.D.G., 2009. Role of plant hormones in plant defence responses. Plant Molecular Biology 69, 473–488.

Berkey, R., Bendigeri, D., Xiao, S., 2012. Sphingolipids and Plant Defense/Disease: The "Death" Connection and Beyond. Frontiers in Plant Science 3.

Betsuyaku, S., Katou, S., Takebayashi, Y., Sakakibara, H., Nomura, N., Fukuda, H., 2018. Salicylic Acid and Jasmonic Acid Pathways are Activated in Spatially Different Domains Around the Infection Site During Effector-Triggered Immunity in *Arabidopsis thaliana*. Plant and Cell Physiology 59, 8–16.

Bjornson, M., Zipfel, C., 2021. Plant immunity: Crosstalk between plant immune receptors. Current Biology 31, R796–R798.

Block, A., Schmelz, E., Jones, J.B., Klee, H.J., 2005. Coronatine and salicylic acid: the battle between *Arabidopsis* and *Pseudomonas* for phytohormone control. Molecular Plant Pathology 6, 79–83.

Boyes, D.C., Nam, J., Dangl, J.L., 1998. The *Arabidopsis thaliana* RPM1 disease resistance gene product is a peripheral plasma membrane protein that is degraded coincident with the hypersensitive response. Proceedings of the National Academy of Sciences U.S.A. 95, 15849–15854.

Boyle, P.C., Martin, G.B., 2015. Greasy tactics in the plant-pathogen molecular arms race. Journal of Experimental Botany 66, 1607–1616.

Brasseur, R., Killian, J.A., De Kruijff, B., Ruysschaert, J.M., 1987. Conformational analysis of gramicidin-gramicidin interactions at the air/water interface suggests that gramicidin aggregates into tube-like structures similar as found in the gramicidin-induced hexagonal HII phase. Biochimica et Biophysica Acta (BBA) - Biomembranes 903, 11–17.

Brooks, D.M., Bender, C.L., Kunkel, B.N., 2005. The *Pseudomonas syringae* phytotoxin coronatine promotes virulence by overcoming salicylic acid-dependent defences in *Arabidopsis thaliana*. Molecular Plant Pathology 6, 629–639.

Buell, C.R., Joardar, V., Lindeberg, M., Selengut, J., Paulsen, I.T., Gwinn, M.L., Dodson, R.J., Deboy, R.T., Durkin, A.S., Kolonay, J.F., Madupu, R., Daugherty, S., Brinkac, L., Beanan, M.J., Haft, D.H., Nelson, W.C., Davidsen, T., Zafar, N., Zhou, L., Liu, J., Yuan, Q., Khouri, H., Fedorova, N., Tran, B., Russell, D., Berry, K., Utterback, T., Van Aken, S.E., Feldblyum, T.V., D'Ascenzo, M., Deng, W.-L., Ramos, A.R., Alfano, J.R., Cartinhour, S., Chatterjee, A.K., Delaney, T.P., Lazarowitz, S.G., Martin, G.B., Schneider, D.J., Tang, X., Bender, C.L., White, O., Fraser, C.M., Collmer, A., 2003. The complete genome sequence of the *Arabidopsis* and tomato pathogen *Pseudomonas syringae* pv. *tomato* DC3000. Proceedings of the National Academy of Sciences U.S.A. 100, 10181–10186.

Cacas, J.-L., Buré, C., Grosjean, K., Gerbeau-Pissot, P., Lherminier, J., Rombouts, Y., Maes, E., Bossard, C., Gronnier, J., Furt, F., Fouillen, L., Germain, V., Bayer, E., Cluzet, S., Robert, F., Schmitter, J.-M., Deleu, M., Lins, L., Simon-Plas, F., Mongrand, S., 2016. Revisiting plant plasma membrane lipids in tobacco: A focus on sphingolipids. Plant Physiology 170, 367–384.

Chen, M., Markham, J.E., Dietrich, C.R., Jaworski, J.G., Cahoon, E.B., 2008. Sphingolipid long-chain base hydroxylation is important for growth and regulation of sphingolipid content and composition in *Arabidopsis*. The Plant Cell 20, 1862–1878.

Contreras, F.-X., Sot, J., Alonso, A., Goñi, F.M., 2006. Sphingosine Increases the Permeability of Model and Cell Membranes. Biophysical Journal 90, 4085–4092.

Cordelier, S., Crouzet, J., Gilliard, G., Dorey, S., Deleu, M., Dhondt-Cordelier, S., 2022. Deciphering the role of plant plasma membrane lipids in response to invasion patterns: how could biology and biophysics help? Journal of Experimental Botany 73, 2765-2784.

Coursol, S., Fromentin, J., Noirot, E., Brière, C., Robert, F., Morel, J., Liang, Y.-K., Lherminier, J. and Simon-Plas, F., 2015. Long-chain bases and their phosphorylated derivatives differentially regulate cryptogein-induced production of reactive oxygen species in tobacco (*Nicotiana tabacum*) BY-2 cells. New Phytologist 205: 1239-1249.

Couto, D., Zipfel, C., 2016. Regulation of pattern recognition receptor signalling in plants. Nature Review Immunology 16, 537–552.

Debener, T., Lehnackers, H., Arnold, M., Dangl, J.L., 1991. Identification and molecular mapping of a single *Arabidopsis thaliana* locus determining resistance to a phytopathogenic *Pseudomonas syringae* isolate. The Plant Journal 1, 289–302.

Deboever, E., Van Aubel, G., Rondelli, V., Koutsioubas, A., Mathelie-Guinlet, M., Dufrene, Y.F., Ongena, M., Lins, L., Van Cutsem, P., Fauconnier, M., Deleu, M., 2022. Modulation of plant plasma membrane structure by exogenous fatty acid hydroperoxide is a potential perception mechanism for their eliciting activity. Plant Cell & Environment 45, 1082–1095.

Deleu, M., Crowet, J.-M., Nasir, M.N., Lins, L., 2014. Complementary biophysical tools to investigate lipid specificity in the interaction between bioactive molecules and the plasma membrane: A review. Biochimica et Biophysica Acta (BBA) - Biomembranes 1838, 3171–3190.

Deleu, M., Deboever, E., Nasir, M.N., Crowet, J.-M., Dauchez, M., Ongena, M., Jijakli, H., Fauconnier, M.-L., Lins, L., 2019. Linoleic and linolenic acid hydroperoxides interact differentially with biomimetic plant membranes in a lipid specific manner. Colloids and Surfaces B: Biointerfaces 175, 384–391.

Deleu, M., Lorent, J., Lins, L., Brasseur, R., Braun, N., El Kirat, K., Nylander, T., Dufrêne, Y.F., Mingeot-Leclercq, M.-P., 2013. Effects of surfactin on membrane models displaying lipid phase separation. Biochimica et Biophysica Acta (BBA) - Biomembranes 1828, 801–815.

Deleu, M., Paquot, M., Nylander, T., 2008. Effect of Fengycin, a Lipopeptide Produced by *Bacillus subtilis*, on Model Biomembranes. Biophysical Journal 94, 2667–2679.

Desveaux, D., Singer, AU., Dangl JL., 2006. Type III effector proteins: doppelgangers of bacterial virulence. Current Opinion in Plant Biology 9, 376-382.

Dinic, J., Biverståhl, H., Mäler, L., Parmryd, I., 2011. Laurdan and di-4-ANEPPDHQ do not respond to membrane-inserted peptides and are good probes for lipid packing. Biochimica Biophysica Acta 1808, 298–306.

Dodds, P.N., Rafiqi, M., Gan, P.H.P., Hardham, A.R., Jones, D.A. and Ellis, J.G. (2009), Effectors of biotrophic fungi and oomycetes: pathogenicity factors and triggers of host resistance. New Phytologist, 183: 993-1000.

Ducarme, P., Rahman, M., Brasseur, R., 1998. IMPALA: A simple restraint field to simulate the biological membrane in molecular structure studies. PROTEINS: Structure, Function, and Genetics 30:357–371

Fischer, C.L., Drake, D.R., Dawson, D.V., Blanchette, D.R., Brogden, K.A., Wertz, P.W., 2012. Antibacterial activity of sphingoid bases and fatty acids against gram-positive and gram-negative bacteria. Antimicrobial Agents and Chemotherapy 56, 1157–1161.

Franche, A., Fayeulle, A., Lins, L., Billamboz, M., Pezron, I., Deleu, M., Léonard, E., 2020. Amphiphilic azobenzenes: Antibacterial activities and biophysical investigation of their interaction with bacterial membrane lipids. Bioorganic Chemistry 94, 103399.

Furlan, A.L., Laurin, Y., Botcazon, C., Rodríguez-Moraga, N., Rippa, S., Deleu, M., Lins, L., Sarazin, C., Buchoux, S., 2020. Contributions and limitations of biophysical approaches to study of the interactions between amphiphilic molecules and the plant plasma membrane. Plants 9, 648.

Gassmann, W., Hinsch, M.E., Staskawicz, B.J., 1999. The *Arabidopsis* RPS4 bacterial-resistance gene is a member of the TIR-NBS-LRR family of disease-resistance genes. The Plant Journal 20, 265–277.

Gerbeau-Pissot, P., Der, C., Thomas, D., Anca, I.-A., Grosjean, K., Roche, Y., Perrier-Cornet, J.-M., Mongrand, S., Simon-Plas, F., 2014. Modification of plasma membrane organization in tobacco cells elicited by cryptogein. Plant Physiology 164, 273–286.

Glenz, R., Kaiping, A., Göpfert, D., Weber, H., Lambour, B., Sylvester, M., Fröschel, C., Mueller, M.J., Osman, M., Waller, F., 2022. The major plant sphingolipid long chain base phytosphingosine inhibits growth of bacterial and fungal plant pathogens. Scientific Reports 12, 1081.

Glenz, R., Schmalhaus, D., Krischke, M., Mueller, M.J., Waller, F., 2019. Elevated levels of phosphorylated sphingobases do not antagonize sphingobase- or fumonisin B1-induced plant cell death. Plant and Cell Physiology 60, 1109–1119.

Grant, M., Godiard, L., Straube, E., Ashfield, T., Lewald, J., Sattler, A., Innes, R., Dangl, J., 1995. Structure of the *Arabidopsis* RPM1 gene enabling dual specificity disease resistance. Science 269, 843–846.

Grennan, A.K., 2007. Lipid Rafts in Plants. Plant Physiology 143, 1083–1085.

Gronnier, J., Gerbeau-Pissot, P., Germain, V., Mongrand, S., Simon-Plas, F., 2018. Divide and rule: Plant plasma membrane organization. Trends in Plant Science 23, 899–917.

Gronnier, J., Germain, V., Gouguet, P., Cacas, J.-L., Mongrand, S., 2016. GIPC: Glycosyl Inositol Phospho Ceramides, the major sphingolipids on earth. Plant Signaling & Behavior 11, e1152438.

Guan, R., Su, J., Meng, X., Li, S., Liu, Y., Xu, J., Zhang, S., 2015. Multilayered regulation of ethylene induction plays a positive role in *Arabidopsis* resistance against *Pseudomonas syringae*. Plant Physiology 169, 299–312.

Gutiérrez-Nájera, N.A., Saucedo-García, M., Noyola-Martínez, L., Vázquez-Vázquez, C., Palacios-Bahena, S., Carmona-Salazar, L., Plasencia, J., El-Hafidi, M., Gavilanes-Ruiz, M., 2020. Sphingolipid effects on the plasma membrane produced by addition of fumonisin B1 to maize embryos. Plants 9, 150.

Hao, H., Fan, L., Chen, T., Li, R., Li, X., He, Q., Botella, M.A., Lin, J., 2014. Clathrin and membrane microdomains cooperatively regulate RbohD dynamics and activity in *Arabidopsis*. Plant Cell 26, 1729–1745.

Heerklotz, H., Seelig, J., 2000. Titration calorimetry of surfactant–membrane partitioning and membrane solubilization. Biochimica et Biophysica Acta (BBA) - Biomembranes 1508, 69–85.

Henry, E., Yadeta, K.A., Coaker, G., 2013. Recognition of bacterial plant pathogens: local, systemic and transgenerational immunity. New Phytologist 199, 908–915.

Henry, G., Deleu, M., Jourdan, E., Thonart, P., Ongena, M., 2011, The bacterial lipopeptide surfactin targets the lipid fraction of the plant plasma membrane to trigger immune-related defence responses. Cellular Microbiology 13, 1824-1837.

Herrfurth, C., Feussner, I., 2020. Quantitative jasmonate profiling using a high-throughput UPLC-NanoESI-MS/MS method. In: Champion, A., Laplaze, L. (eds) Jasmonate in Plant Biology. Methods in Molecular Biology, vol 2085. Humana, New York, NY.

Hicks, S.W., Galán, J.E., 2013. Exploitation of eukaryotic subcellular targeting mechanisms by bacterial effectors. Nature Reviews Microbiology 11, 316–326.

Huby, E., Napier, J.A., Baillieul, F., Michaelson, L.V., Dhondt-Cordelier, S., 2020. Sphingolipids: towards an integrated view of metabolism during the plant stress response. New Phytologist 225, 659–670.

Ishikawa, T., Aki, T., Yanagisawa, S., Uchimiya, H., Kawai-Yamada, M., 2015. Overexpression of BAX INHIBITOR-1 links plasma membrane microdomain proteins to stress. Plant Physiology 169, 1333–1343.

Jones, J.D.G., Dangl, J.L., 2006. The plant immune system. Nature 444, 323–329.

Kadota, Y., Liebrand, T.W.H., Goto, Y., Sklenar, J., Derbyshire, P., Menke, F.L.H., Torres, M., Molina, A., Zipfel, C., Coaker, G., Shirasu, K., 2019. Quantitative phosphoproteomic analysis reveals common regulatory mechanisms between effector- and PAMP-triggered immunity in plants. New Phytologist 221, 2160–2175.

Kamoun, S., 2006. A catalogue of the effector secretome of plant pathogenic oomycetes. Annual Review of Phytopathology 44, 41-60.

Kato, H., Nemoto, K., Shimizu, M., Abe, A., Asai, S., Ishihama, N., Matsuoka, S., Daimon, T., Ojika, M., Kawakita, K., Onai, K., Shirasu, K., Yoshida, M., Ishiura, M., Takemoto, D., Takano, Y., Terauchi, R., 2022. Recognition of pathogen-derived sphingolipids in Arabidopsis, Science 376, 857-860.

Kawasaki, T., Nam, J., Boyes, D.C., Holt, B.F., Hubert, D.A., Wiig, A., Dangl, J.L., 2005. A duplicated pair of *Arabidopsis* RING-finger E3 ligases contribute to the RPM1- and RPS2-mediated hypersensitive response: Transmembrane RING-E3 ligases and the HR. The Plant Journal 44, 258–270.

Kimberlin, A.N., Han, G., Chen, M., Cahoon, R.E., Luttgeharm, K.D., Stone, J.M., Markham, J.E., Dunn, T.M., Cahoon, E.B., 2016. ORM expression alters sphingolipid homeostasis and differentially affects ceramide synthase activities. Plant Physiology 172, 889-900.

Klemptner, R.L., Sherwood, J.S., Tugizimana, F., Dubery, I.A., Piater, L.A., 2014. Ergosterol, an orphan fungal microbe-associated molecular pattern (MAMP): Ergosterol as a MAMP. Molecular Plant Pathology 15, 747–761.

König, S., Feussner, K., Schwarz, M., Kaever, A., Iven, T., Landesfeind, M., Ternes, P., Karlovsky, P., Lipka, V., Feussner, I., 2012. *Arabidopsis* mutants of sphingolipid fatty acid α-hydroxylases accumulate ceramides and salicylates. New Phytologist 196, 1086–1097.

König, S., Gömann, J., Zienkiewicz, A., Zienkiewicz, K., Meldau, D., Herrfurth, C., Feussner, I., 2021. Sphingolipid-induced programmed cell death is a salicylic acid and EDS1-dependent phenotype in *Arabidopsis*. Biochemistry 63, 317-325.

Lebecque, S., Crowet, J.-M., Lins, L., Delory, B.M., du Jardin, P., Fauconnier, M.-L., Deleu, M., 2018. Interaction between the barley allelochemical compounds gramine and hordenine and artificial lipid bilayers mimicking the plant plasma membrane. Scientific Reports 8, 9784.

Lee, C.C., Wood, M.D., Ng, K., Andersen, C.B., Liu, Y., Luginbühl, P., Spraggon, G., Katagiri, F., 2004. Crystal structure of the type III effector AvrB from *Pseudomonas syringae*. Structure 12, 487–494.

Lee, D., Bourdais, G., Yu, G., Robatzek, S., Coaker, G., 2015. Phosphorylation of the plant immune regulator RPM1-INTERACTING PROTEIN4 enhances plant plasma membrane H + -ATPase activity and inhibits flagellin-triggered immune responses in *Arabidopsis*. Plant Cell 27, 2042–2056.

Lenarčič, T., Albert, I., Böhm, H., Hodnik, V., Pirc, K., Zavec, A.B., Podobnik, M., Pahovnik, D., Žagar, E., Pruitt, R., Greimel, P., Yamaji-Hasegawa, A., Kobayashi, T., Zienkiewicz, A., Gömann, J., Mortimer, J.C., Fang, L., Mamode-Cassim, A., Deleu, M., Lins, L., Oecking, C., Feussner, I., Mongrand, S., Anderluh, G., Nürnberger, T., 2017. Eudicot plant-specific sphingolipids determine host selectivity of microbial NLP cytolysins. Science 358, 1431–1434.

Lherminier, J., Elmayan, T., Fromentin, J., Elaraqui, K.T., Vesa, S., Morel, J., Verrier, J.-L., Cailleteau, B., Blein, J.-P., Simon-Plas, F., 2009. NADPH oxidase-mediated reactive oxygen species production: Subcellular localization and reassessment of its role in plant defense. Molecular Plant-Microbe Interactions 22, 868–881.

Li, N., Han, X., Feng, D., Yuan, D., Huang, L.-J., 2019. Signaling crosstalk between salicylic acid and ethylene/jasmonate in plant defense: Do we understand what they are whispering? International Journal of Molecular Sciences 20, 671.

Lins, L., Brasseur, R., Malaisse, W.J., 1995. Conformational analysis of non-sulfonylurea hypoglycemic agents of the meglitinide family. Biochemical Pharmacology 50, 1879–1884.

Luttgeharm, K.D., Kimberlin, A.N., Cahoon, E.B., 2016. Plant sphingolipid metabolism and function, in: Nakamura, Y., Li-Beisson, Y. (Eds.), Lipids in Plant and Algae Development. Springer International Publishing, Cham, pp. 249–286.

Luzuriaga-Loaiza, W.P., Schellenberger, R., De Gaetano, Y., Obounou Akong, F., Villaume, S., Crouzet, J., Haudrechy, A., Baillieul, F., Clément, C., Lins, L., Allais, F., Ongena, M., Bouquillon, S., Deleu, M., Dorey, S., 2018. Synthetic rhamnolipid bolaforms trigger an innate immune response in *Arabidopsis thaliana*. Scientific Reports 8, 8534.

1031 Mackey, D., Belkhadir, Y., Alonso, J.M., Ecker, J.R., Dangl, J.L., 2003. *Arabidopsis* RIN4 is a target of
1032 the type III virulence effector AvrRpt2 and modulates RPS2-mediated resistance. Cell 112, 379–389.
1033 Mackey, D., Holt III, B.F., Wiig, A., Dangl, J.L., 2002. RIN4 interacts with *Pseudomonas syringae* type
1034 III effector molecules and is required for RPM1-mediated resistance in *Arabidopsis*. Cell 108, 743–
1035 754.
1036 Magazzù, A., Marcuello, C., 2023. Investigation of soft matter nanomechanics by atomic force
1037 microscopy and optical tweezers: A comprehensive review. Nanomaterials 13, 963.
1038 Magnin-Robert, M., Le Bourse, D., Markham, J.E., Dorey, S., Clément, C., Baillieul, F., Dhondt-
1039 Cordelier, S., 2015. Modifications of sphingolipid content affect tolerance to hemibiotrophic and
1040 necrotrophic pathogens by modulating plant defense responses in *Arabidopsis*. Plant Physiology 169,
1041 2255-2274.
1042 Mamode Cassim, A., Gouguet, P., Gronnier, J., Laurent, N., Germain, V., Grison, M., Boutté, Y.,
1043 Gerbeau-Pissot, P., Simon-Plas, F., Mongrand, S., 2019. Plant lipids: Key players of plasma
1044 membrane organization and function. Progress in Lipid Research 73, 1–27.
1045 Marsh, D., 1996. Lateral pressure in membranes. Biochimica et Biophysica Acta (BBA) - Reviews on
1046 Biomembranes 1286, 183–223.
1047 Mongrand, S., Morel, J., Laroche, J., Claverol, S., Carde, J.-P., Hartmann, M.-A., Bonneu, M., Simon-
1048 Plas, F., Lessire, R., Bessoule, J.-J., 2004. Lipid rafts in higher plant cells: purification and
1049 characterization of triton x-100-insoluble microdomains from tobacco plasma membrane. Journal
1050 Biological Chemistry 279, 36277–36286.
1051 Moore, R.A., Starratt, A.N., Ma, S.-W., Morris, V.L., Cuppels, D.A., 1989. Identification of a chromosomal
1052 region required for biosynthesis of the phytotoxin coronatine by *Pseudomonas syringae* pv. tomato.
1053 Canadian Journal of Microbiology 35, 910–917.
1054 Mur, L.A.J., Kenton, P., Atzorn, R., Miersch, O., Wasternack, C., 2006. The outcomes of concentration-
1055 specific interactions between salicylate and jasmonate signaling include synergy, antagonism, and
1056 oxidative stress leading to cell death. Plant Physiology 140, 249–262.
1057 Nagano, M., Ishikawa, T., Fujiwara, M., Fukao, Y., Kawano, Y., Kawai-Yamada, M., Shimamoto, K.,
1058 2016. Plasma membrane microdomains are essential for Rac1-RbohB/H-mediated immunity in rice.
1059 The Plant Cell 28, 1966–1983.
1060 Nasir, M.N., Crowet, J.-M., Lins, L., Obounou Akong, F., Haudrechy, A., Bouquillon, S., Deleu, M., 2016.
1061 Interactions of sugar-based bolaamphiphiles with biomimetic systems of plasma membranes.
1062 Biochimie 130, 23–32.
1063 Nasir, M.N., Thawani, A., Kouzayha, A., Besson, F., 2010. Interactions of the natural antimicrobial
1064 mycosubtilin with phospholipid membrane models. Colloids and Surfaces B: Biointerfaces 78, 17–23.
1065 Ngou, B.P.M., Ahn, H.-K., Ding, P., Jones, J.D.G., 2021. Mutual potentiation of plant immunity by cell-
1066 surface and intracellular receptors. Nature 592, 110–115.
1067 Nimchuk, Z., Marois, E., Kjemtrup, S., Leister, R.T., Katagiri, F., Dangl, J.L., 2000. Eukaryotic fatty
1068 acylation drives plasma membrane targeting and enhances function of several type III effector proteins
1069 from *Pseudomonas syringae*. Cell 101, 353–363.
1070 Parasassi, T., De Stasio, G., Ravagnan, G., Rusch, R.M., Gratton, E., 1991. Quantitation of lipid phases
1071 in phospholipid vesicles by the generalized polarization of Laurdan fluorescence. Biophysical Journal
1072 60, 179–189.
1073 Pata, M.O., Hannun, Y.A., Ng, C.K.-Y., 2010. Plant sphingolipids: decoding the enigma of the Sphinx:
1074 Tansley review. New Phytologist 185, 611–630.
1075 Peer, M., Bach, M., Mueller, M.J., Waller, F., 2011. Free sphingobases induce RBOHD-dependent
1076 reactive oxygen species production in *Arabidopsis* leaves. FEBS Letters 585, 3006–3010.
1077 Pierre M., Traverso J.A., Boisson B., Domenichini S., Bouchez D., Giglione C., Meinnel T., 2007. *N*-
1078 myristoylation regulates the SnRK1 pathway in *Arabidopsis*, The Plant Cell 19, 2804–2821
1079 Pottinger, S.E., Innes, R.W., 2020. RPS5-Mediated Disease Resistance: Fundamental Insights and
1080 Translational Applications. Annual Review of Phytopathology 58, 139-160.
1081 Rondelli, V., Mollica, L., Koutsioubas, A., Nasir, N., Trapp, M., Deboever, E., Brocca, P., Deleu, M.,
1082 2022. Carbohydrate-carbohydrate interaction drives the preferential insertion of dirhamnolipid into
1083 glycosphingolipid enriched membranes. Journal of Colloid and Interface Science, 616, 739-748.
1084 Rossard, S., Roblin, G., Atanassova, R., 2010. Ergosterol triggers characteristic elicitation steps in Beta
1085 vulgaris leaf tissues. Journal of Experimental Botany 61, 1807–1816.
1086 Saijo, Y., Loo, E.P. iian, 2020. Plant immunity in signal integration between biotic and abiotic stress
1087 responses. New Phytologist 225, 87–104.
1088 Saile, S.C., Ackermann, F.M., Sunil, S., Keicher, J., Bayless, A., Bonardi, V., Wan, L., Doumane, M.,
1089 Stöbbe, E., Jaillais, Y., Caillaud, M.-C., Dangl, J.L., Nishimura, M.T., Oecking, C. and El Kasmi, F.

2021. Arabidopsis ADR1 helper NLR immune receptors localize and function at the plasma membrane in a phospholipid dependent manner. New Phytologist 232: 2440-2456.

Saucedo-García, M., González-Solís, A., Rodríguez-Mejía, P., Lozano-Rosas, G., Olivera-Flores, T. de J., Carmona-Salazar, L., Guevara-García, A.A., Cahoon, E.B., Gavilanes-Ruíz, M., 2023. Sphingolipid long-chain base signaling in compatible and non-compatible plant pathogen interactions in *Arabidopsis*. International Journal of Molecular Sciences 24, 4384.

Saucedo-García, M., Guevara-García, A., González-Solís, A., Cruz-García, F., Vázquez-Santana, S., Markham, J.E., Lozano-Rosas, M.G., Dietrich, C.R., Ramos-Vega, M., Cahoon, E.B., Gavilanes-Ruíz, M., 2011. MPK6, sphinganine and the LCB2a gene from serine palmitoyltransferase are required in the signaling pathway that mediates cell death induced by long chain bases in *Arabidopsis*. New Phytologist 191, 943–957.

Schellenberger, R., Crouzet, J., Nickzad, A., Shu, L.-J., Kutschera, A., Gerster, T., Borie, N., Dawid, C., Cloutier, M., Villaume, S., Dhondt-Cordelier, S., Hubert, J., Cordelier, S., Mazeyrat-Gourbeyre, F., Schmid, C., Ongena, M., Renault, J.-H., Haudrechy, A., Hofmann, T., Baillieul, F., Clément, C., Zipfel, C., Gauthier, C., Déziel, E., Ranf, S., Dorey, S., 2021. Bacterial rhamnolipids and their 3-hydroxyalkanoate precursors activate *Arabidopsis* innate immunity through two independent mechanisms. Proceedings of the National Academy of Sciences U.S.A. 118, e2101366118.

Schindelin, J., Arganda-Carreras, I., Frise, E., Kaynig, V., Longair, M., Pietzsch, T., Preibisch, S., Rueden, C., Saalfeld, S., Schmid, B., Tinevez, J.-Y., White, D.J., Hartenstein, V., Eliceiri, K., Tomancak, P., Cardona, A., 2012. Fiji: an open-source platform for biological-image analysis. Nature Methods 9, 676–682.

Shi, L., Bielawski, J., Mu, J., Dong, H., Teng, C., Zhang, J., Yang, X., Tomishige, N., Hanada, K., Hannun, Y.A., 2007. Involvement of sphingoid bases in mediating reactive oxygen intermediate production and programmed cell death in *Arabidopsis*. Cell Research 17, 1030.

Smith, J.M., Heese, A. Rapid bioassay to measure early reactive oxygen species production in *Arabidopsis* leave tissue in response to living *Pseudomonas syringae*. Plant Methods **10**, 6 (2014).

Ternes, P., Feussner, K., Werner, S., Lerche, J., Iven, T., Heilmann, I., Riezman, H., Feussner, I., 2011. Disruption of the ceramide synthase LOH1 causes spontaneous cell death in *Arabidopsis thaliana*. New Phytologist 192, 841–854.

Torres, M.A., 2010. ROS in biotic interactions. Physiologia Plantarum 138, 414–429.

Torres, M.A., Jones, J.D.G., Dangl, J.L., 2005. Pathogen-induced, NADPH oxidase–derived reactive oxygen intermediates suppress spread of cell death in *Arabidopsis thaliana*. Nature Genetics 37, 1130–1134.

Warren, R.F., Henk, A., Mowery, P., Holub, E., Innes, R.W., 1998. A mutation within the leucine-rich repeat domain of the *Arabidopsis* disease resistance gene RPS5 partially suppresses multiple bacterial and downy mildew resistance genes. The Plant Cell 10, 1439–1452.

Wei, H.-L., Zhang, W., Collmer, A., 2018. Modular study of the type III effector repertoire in *Pseudomonas syringae* pv. *tomato* DC3000 reveals a matrix of effector interplay in pathogenesis. Cell Reports 23, 1630–1638.

Whalen, M.C., Innes, R.W., Bent, A.F., Staskawicz, B.J., 1991. Identification of *Pseudomonas syringae* pathogens of *Arabidopsis* and a bacterial locus determining avirulence on both *Arabidopsis* and soybean. The Plant Cell 3, 49–59.

Wirthmueller, L., Zhang, Y., Jones, J.D.G., Parker, J.E., 2007. Nuclear accumulation of the *Arabidopsis* immune receptor RPS4 is necessary for triggering EDS1-dependent defense. Current Biology 17, 2023–2029.

Xin, X.-F., Kvitko, B., He, S.Y., 2018. *Pseudomonas syringae*: what it takes to be a pathogen. Nature Reviews Microbiology 16, 316–328.

Yoo, SD., Cho, YH., Sheen, J., 2007. *Arabidopsis* mesophyll protoplasts: a versatile cell system for transient gene expression analysis. Nature Protocols 2, 1565–1572.

Yuan, M., Jiang, Z., Bi, G., Nomura, K., Liu, M., Wang, Y., Cai, B., Zhou, J.-M., He, S.Y., Xin, X.-F., 2021. Pattern-recognition receptors are required for NLR-mediated plant immunity. Nature 592, 105–109.

Zheng, X., Spivey, N.W., Zeng, W., Liu, P.-P., Fu, Z.Q., Klessig, D.F., He, S.Y., Dong, X., 2012. Coronatine promotes *Pseudomonas syringae* virulence in plants by activating a signaling cascade that inhibits salicylic acid accumulation. Cell Host & Microbe 11, 587–596.

Zhou, N., Tootle, T.L., Tsui, F., Klessig, D.F., Glazebrook, J., 1998. PAD4 functions upstream from salicylic acid to control defense responses in *Arabidopsis*. The Plant Cell 10, 1021–1030.

1149 **Figure legends**

1150 **FIGURE 1 Effect of co-infiltration of *Pst* and d18:0 on cell death.** (A)
1151 Representative leaves of Col-0 WT 48 hours after infiltration with either *Pst* DC3000,
1152 *Pst AvrRpm1*, *Pst AvrRpt2*, *Pst AvrRps4* alone or co-infiltrated with d18:0. The
1153 experiment was repeated at least 5 times with similar results (n=5). (B) Ion leakage
1154 measurements over 24 hours following infiltration with *Pst AvrRpm1*, *Pst AvrRpt2* or
1155 *Pst AvrRps4*, alone or with d18:0. Data are reported as means ± SD (n=3). The
1156 experiment was repeated three times with similar results.

1157

1158 **FIGURE 2 *In vitro* and *in planta* bacterial growth in presence of sphinganine.** (A)
1159 Growth rate was estimated from bacterial growth curve data (OD_{600}) over 48 hours,
1160 ±SD in King's B medium. Asterisks indicate significant differences between each
1161 bacterium co-infiltrated with d18:0 or not (Wilcoxon-Mann-Whitney, *, $p<0.05$). (B)
1162 Bacterial growth ±SD (n = 3) at 0 and 48 hpi in *Arabidopsis* WT Col-0 leaves infected
1163 by bacteria alone or with d18:0.

1164

1165 **FIGURE 3 Extracellular ROS production in response to bacterial infection**.
1166 Extracellular ROS production measured in presence of *Pst AvrRpm1*, *Pst AvrRpt2 or*
1167 *Pst AvrRps4* with or without d18:0 in the medium. Data represent the sum of RLU
1168 (Relative Light Units) ± SEM (n = 6) over 90 min. The experiment was performed three
1169 times with similar results. Asterisks indicate significant differences between each
1170 bacterium co-infiltrated with d18:0 or not (Wilcoxon-Mann-Whitney; *, $p<0.05$).

1171

1172 **FIGURE 4 Late plant defense events in response to bacterial infiltration.** *Pst*
1173 DC3000 or *Pst AvrRpm1* were co-infiltrated with or without d18:0. (A) Camalexin was

1174 quantified at 0 and 48 hpi (FW: fresh weight). Different letters indicate significant
1175 differences (ANOVA, $p<0.05$, one way, n=5). (B) Representative leaves of *PR1::GUS*
1176 lines 48 hpi. (C) and (D) Relative expression of *PR1* and *VSP1*, respectively, followed
1177 6 and 48 hpi. Results are expressed as the fold increase in transcript level compared
1178 with the untreated control (0h), referred to as the x1 expression level. Experiments
1179 were repeated 3 times with similar results. (E) and (F) SA and JA-Isoleucine (JA-Ile)
1180 were quantified at 0 and 48 hpi. Different letters indicate significant differences
1181 (ANOVA, $p<0.05$, one way, n = 5).
1182
1183 **FIGURE 5 Involvement of RPM1 in the absence of defense responses**. (A)
1184 Photographs represent symptoms observed 72 hpi in WT, *rpm1-3*, *rpm1-rps2-rin4* and
1185 *RPM1-myc rpm1* lines treated with or without d18:0. (B) Western blot of RPM1 protein
1186 in WT and *RPM1-myc rpm1* line at 2, 6 or 24 hpi. Normalization was carried out with
1187 Actin. NT refers to non-treated samples. All experiments were repeated at least 3 times
1188 with similar results.
1189
1190 **FIGURE 6 Effect of *Pst AvrB* and *Pst AvrPphB* co-infiltration with d18:0 on plant**
1191 **defense responses.** (A) Photographs represent symptoms observed 48 hours after
1192 WT plant infiltration with either *Pst AvrB* or *Pst AvrPphB* alone or with d18:0. The
1193 experiment was repeated at least 3 times with similar results (n = 3). (B) Growth rate
1194 estimated from bacterial growth curve data (OD_{600}) over 48 hours, ±SD in King's B
1195 medium. (C) ROS production measurement in presence of *Pst AvrB* or *AvrPphB* with
1196 or without d18:0. Data represent the sum of RLU (Relative Light Units) ± SEM (n = 6)
1197 over 90 min. Experiments were performed three times with similar results. Asterisks
1198 indicate statistical differences (Wilcoxon-Mann-Whitney; *, $p<0.05$).

1199

1200 **FIGURE 7 *NMT1* expression in response to co-infiltration of bacteria and**
1201 **sphinganine.** Relative expression of *NMT1*, (N-*myristoyltransferase 1*) was followed
1202 at 6, 24 and 48 hpi of *Pst* DC3000 or *Pst AvrRpm1* with or without d18:0. Results are
1203 expressed as the fold increase in transcript level compared with the untreated control
1204 (0h), referred to as the x1 expression level. Experiments were repeated three times
1205 with similar results. Asterisks indicate significant differences between each bacterium
1206 co-infiltrated with d18:0 or not (Wilcoxon-Mann-Whitney; *, $p<0.05$).

1207

1208 **FIGURE 8 Interaction of sphinganine with an implicit modeled bilayer.** (A) The
1209 Impala simulation calculates the energy restraints of a lipid bilayer as d18:0 goes
1210 through it. The X-axis corresponds to the position of the center of mass along the Z-
1211 axis. From left to right: the interface between the bilayer and the aqueous phase
1212 (orange), the interface between the polar head and the alkyl chain (pink) and the center
1213 of the bilayer (green). (B) The most energetically favorable orientation of d18:0 in the
1214 modeled bilayer. The lines represent the same planar surfaces as in A.

1215

1216 **FIGURE 9 Interaction of sphinganine with plant-like liposomes.** (A) Raw data from
1217 ITC experiments at 26°C. Each peak corresponds to a single injection of a 1 mM PLPC,
1218 glucosylceramide and sitosterol (60:20:20, molar ratio) LUV suspension into a solution
1219 containing 20 μM of d18:0. (B) Calculated thermodynamic parameters for this
1220 interaction. These values are means of two independent experiments. K represents
1221 the binding coefficient (the affinity of d18:0 for the LUVs), ΔG represents the molar free
1222 energy, ΔH, the molar enthalpy change, and TΔS, the molar entropy change.

1223

1224 **FIGURE 10 Specificity of sphinganine interaction with various lipids**
1225 **representative of the plant plasma membrane.** (A) Adsorption of d18:0 into
1226 monolayers of plant PM lipids: PLPC, glucosylceramide (GluCer) and β-sitosterol
1227 (Sito). d18:0 was injected at 1.25 μM in a subphase (Tris HCl, 10 mM, pH 7.4),
1228 underneath the lipid monolayer. The maximal insertion pressure (MIP) reflects the
1229 penetration power of d18:0 into the lipid monolayer and the differential Π (dΠ0)
1230 indicates the attracting effect the lipids have on it. (B) Total energies of interaction of
1231 d18:0 alone or with lipids representative of the plant plasma membrane were calculated
1232 with the Hypermatrix docking method. Lipids used were PLPC, GluCer, and Sito.
1233
1234 **Figure 11 Mechanical properties and organization of the plant plasma membrane**
1235 **in response to sphinganine treatment.** (A) to (C) Fluorescence red/green ratio
1236 images by multispectral confocal microscopy of a single-cell PM labeled with di-4-
1237 ANEPPDHQ after control (A), 2 μM d18:0 (B) or 5 μM d18:0 (C) treatment. (D) Red to
1238 green ratio of the PM (RGM) labeled with di-4-ANEPPDHQ treated with control (Ctrl),
1239 2 μM or 5 μM d18:0. The asterisk indicates a significant difference compared to the
1240 control (P value < 0.05). (E) to (G) RGM profile on a 4 μm distance on PM from
1241 protoplasts after control (E), 2 μM d18:0 (F) or 5 μM d18:0 (G) treatment. (H) Variation
1242 of laurdan generalized polarization (ΔGP) measured in PM-mimicking liposomes (50
1243 μM PLPC:Glucosylceramide:b-sitosterol (60:20:20 molar ratio)) at several time points
1244 after control (white bars) and 20 μM d18:0 treatment (grey bars). A positive ΔGP
1245 corresponds to a higher lipid packing within the bilayer. Mean ± SD of two replicates
1246 from four independent experiments. Asterisks indicate statistically significant
1247 differences with control, *P<0.05, **P<0.01, two-way ANOVA and Sidak's multiple
1248 comparison test. (I) Young's modulus measured on mesophyll protoplasts before or

1249 after 5 min incubation of d18:0 at two concentrations. Mean ± SD of at least 50 analyses
1250 from three independent experiments. (J) Monolayer simulations of lipid-d18:0
1251 interactions performed with Big Monolayer where each pixel represents a molecule.
1252 (Left) Plant lipid model with PLPC in green, glucosylceramide (GluCer) in blue and
1253 sitosterol (sito) in orange (60:20:20, molar ratio). (Right) The same lipids after addition
1254 of d18:0 in pink (88% lipids, 12% d18:0).
1255
1256
1257 Supporting Information
1258 **FIGURE S1 Adsorption behaviour of d18:0 into lipid monolayer mimicking plant**
1259 **plasma membrane** (A) Kinetics of d18:0 (1.25 μM in the subphase Tris HCl, 10 mM,
1260 pH 7.4) adsorption to a bare interface or to the lipid monolayer (here the example of
1261 PLPC monolayer) at different initial surface pressures (Π_i). The arrow indicates the
1262 time at which d18:0 was injected underneath the bare interface or the PLPC monolayer.
1263 (B) Surface pressure variation following adsorption of d18:0 versus the initial surface
1264 pressure (Π_i) of the PLPC monolayer.
1265
1266
1267

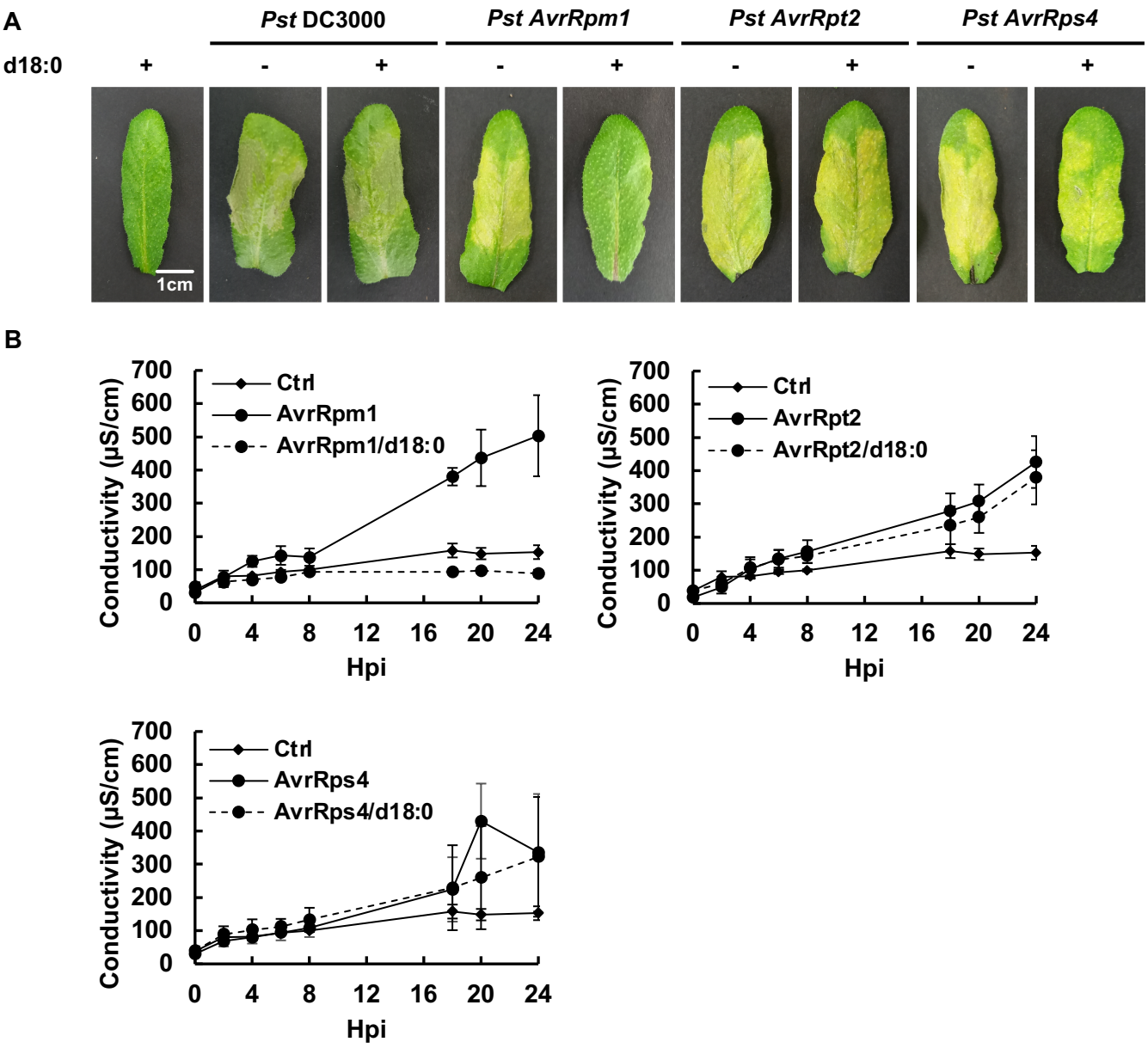

FIGURE 1 Effect of co-infiltration of *Pst* and d18:0 on cell death.
(A) Representative leaves of Col-0 WT 48 hours after infiltration with either *Pst* DC3000, *Pst AvrRpm1*, *Pst AvrRpt2*, *Pst AvrRps4* alone or co-infiltrated with d18:0. The experiment was repeated at least 5 times with similar results (n=5). (B) Ion leakage measurements over 24 hours following infiltration with *Pst AvrRpm1*, *Pst AvrRpt2* or *Pst AvrRps4*, alone or with d18:0. Data are reported as means ± SD (n=3). The experiment was repeated three times with similar results.

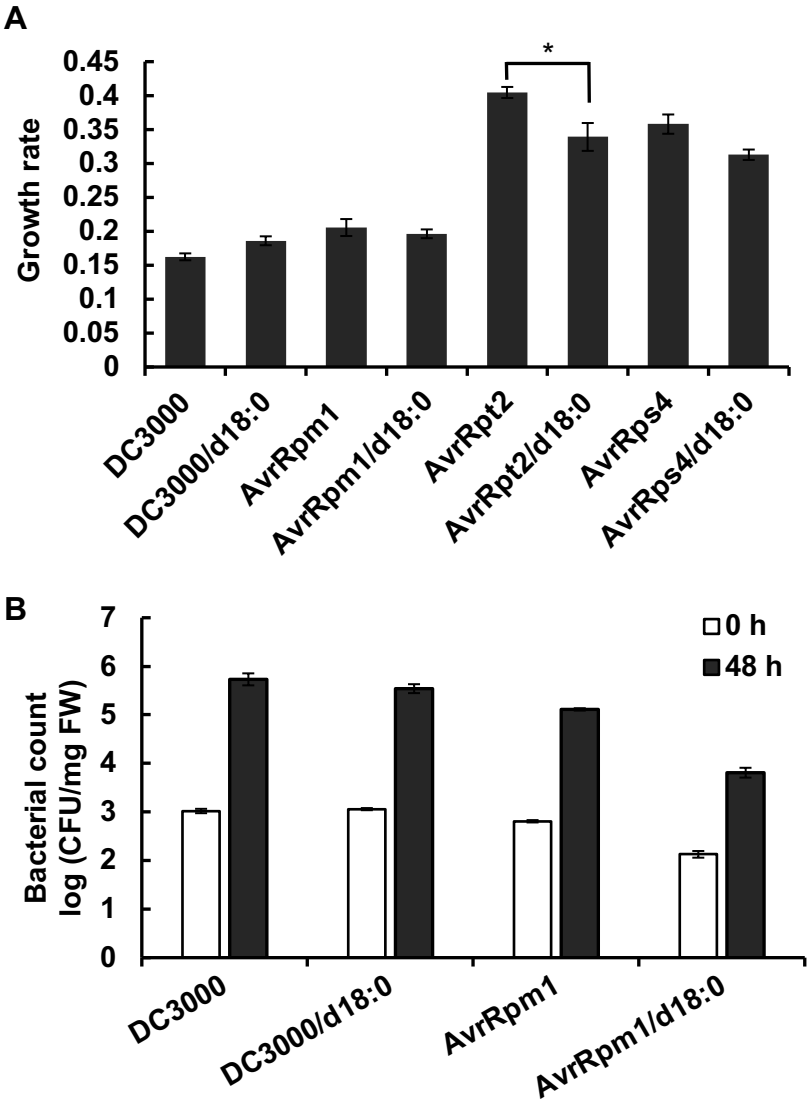

FIGURE 2 *In vitro* and *in planta* bacterial growth in presence of sphinganine. (A) Growth rate was estimated from bacterial growth curve data (OD_{600}) over 48 hours, ±SD in King's B medium. Asterisks indicate significant differences between each bacterium co-infiltrated with d18:0 or not (Wilcoxon-Mann-Whitney, *, $p<0.05$). (B) Bacterial growth ±SD (n = 3) at 0 and 48 hpi in *Arabidopsis* WT Col-0 leaves infected by bacteria alone or with d18:0.

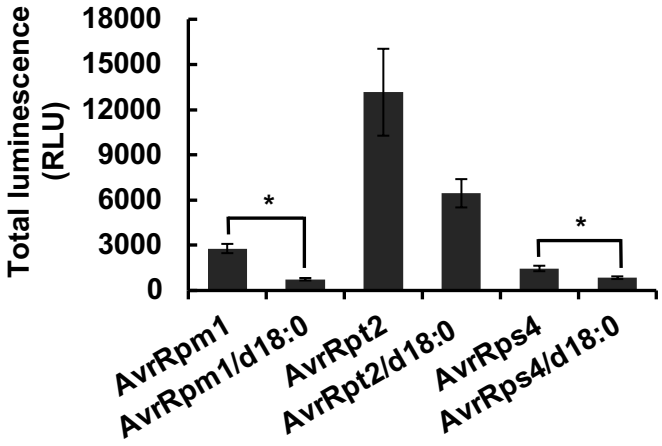

FIGURE 3 Extracellular ROS production in response to bacterial infection.
Extracellular ROS production measured in presence of *Pst AvrRpm1*, *Pst AvrRpt2 or Pst AvrRps4* with or without d18:0 in the medium. Data represent the sum of RLU (Relative Light Units) ± SEM (n = 6) over 90 min. The experiment was performed three times with similar results. Asterisks indicate significant differences between each bacterium co-infiltrated with d18:0 or not (Wilcoxon-Mann-Whitney; *, $p<0.05$).

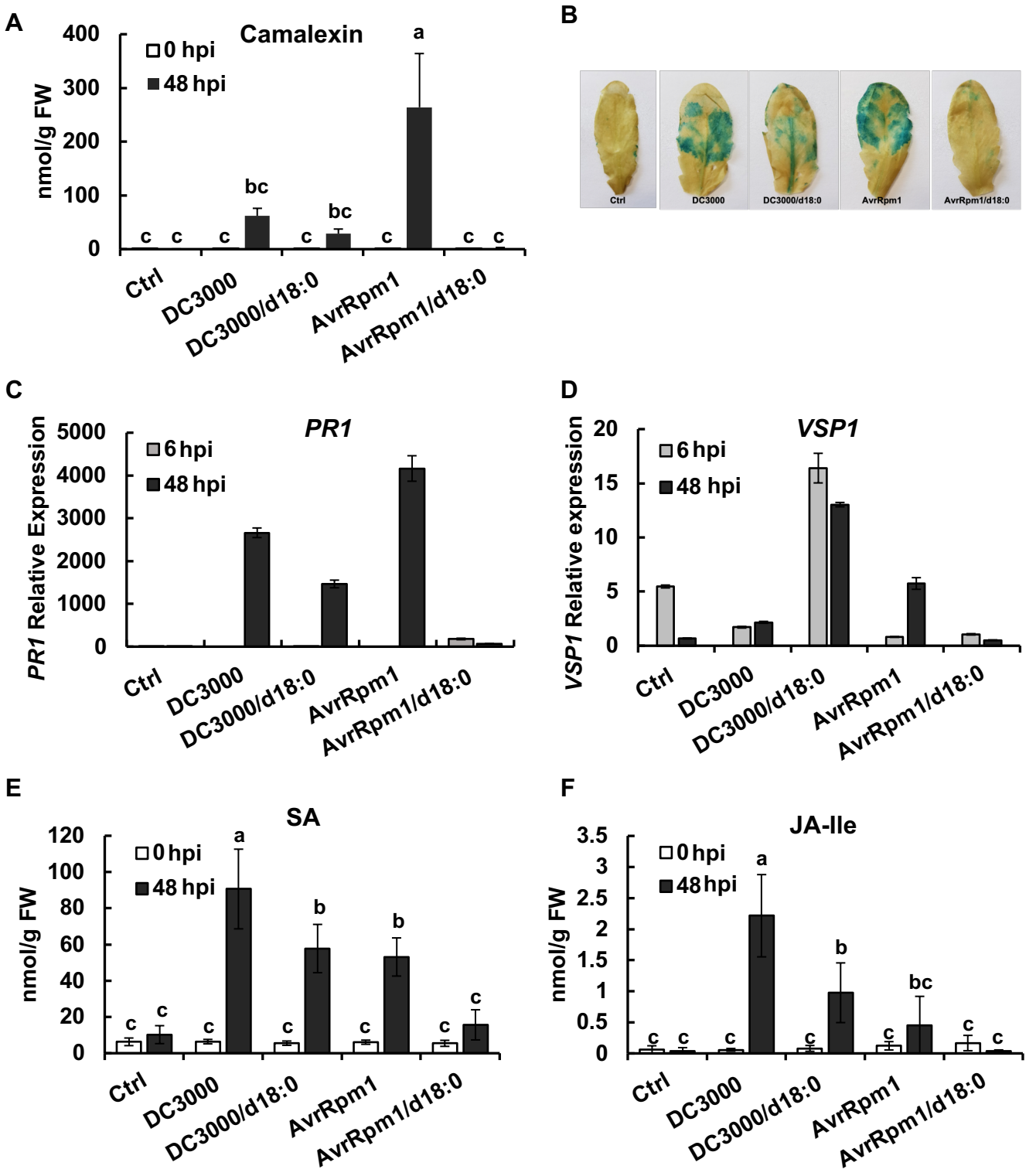

FIGURE 4 Late plant defense events in response to bacterial infiltration.
Pst DC3000 or *Pst AvrRpm1* were co-infiltrated with or without d18:0. (A) Camalexin was quantified at 0 and 48 hpi (FW: fresh weight). Different letters indicate significant differences (ANOVA, $p<0.05$, one way, n=5). (B) Representative leaves of *PR1::GUS* lines 48 hpi. (C) and (D) Relative expression of *PR1* and *VSP1*, respectively, followed 6 and 48 hpi. Results are expressed as the fold increase in transcript level compared with the untreated control (0h), referred to as the x1 expression level. Experiments were repeated 3 times with similar results. (E) and (F) SA and JA-Isoleucine (JA-Ile) were quantified at 0 and 48 hpi. Different letters indicate significant differences (ANOVA, $p<0.05$, one way, n = 5).

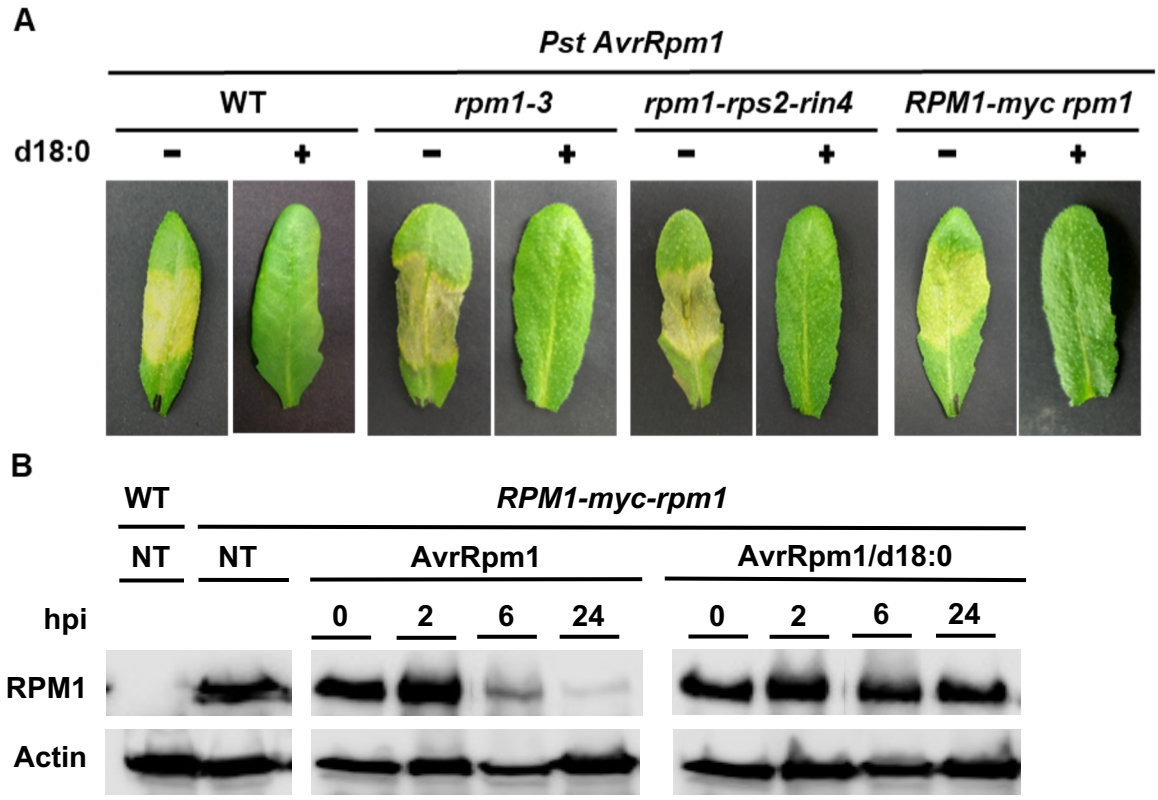

FIGURE 5 Involvement of RPM1 in the absence of defense responses.
(A) Photographs represent symptoms observed 72 hpi in WT, *rpm1-3*, *rpm1-rps2-rin4* and *RPM1-myc rpm1* lines treated with or without d18:0. (B) Western blot of RPM1 protein in WT and *RPM1-myc rpm1* line at 2, 6 or 24 hpi. Normalization was carried out with Actin. NT refers to non-treated samples. All experiments were repeated at least 3 times with similar results.

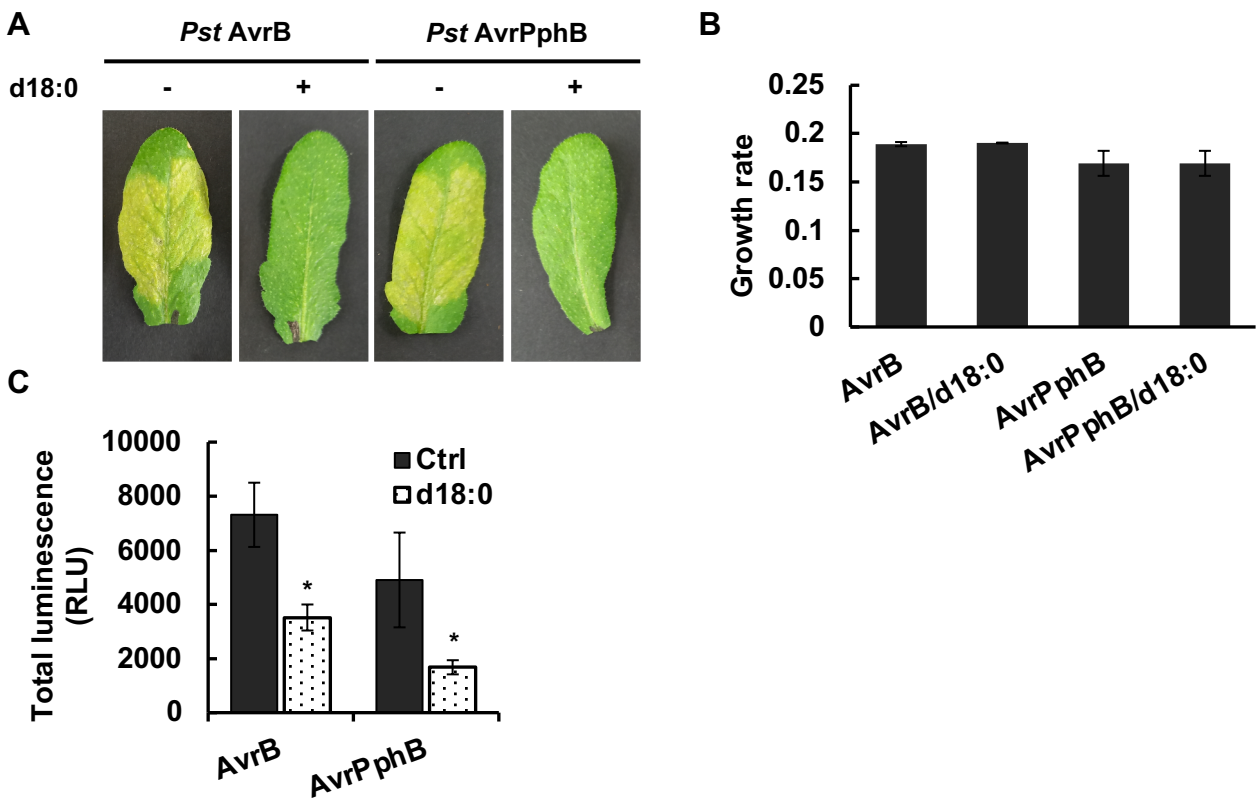

FIGURE 6 Effect of *Pst AvrB* and *Pst AvrPphB* co-infiltration with d18:0 on plant defense responses.

(A) Photographs represent symptoms observed 48 hours after WT plant infiltration with either *Pst AvrB* or *Pst AvrPphB* alone or with d18:0. The experiment was repeated at least 3 times with similar results (n = 3). (B) Growth rate estimated from bacterial growth curve data (OD_{600}) over 48 hours, ±SD in King's B medium. (C) ROS production measurement in presence of *Pst AvrB* or *AvrPphB* with or without d18:0. Data represent the sum of RLU (Relative Light Units) ± SEM (n = 6) over 90 min. Experiments were performed three times with similar results. Asterisks indicate statistical differences (Wilcoxon-Mann-Whitney; *, $p<0.05$).

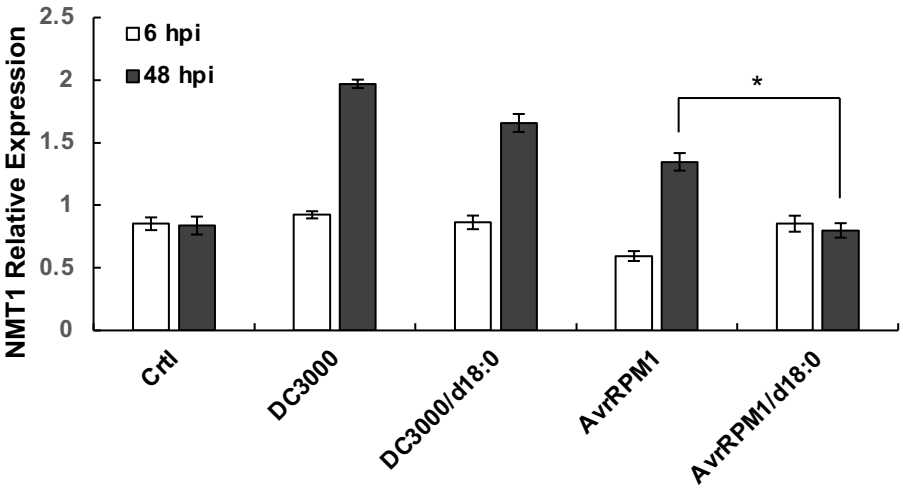

FIGURE 7 *NMT1* expression in response to co-infiltration of bacteria and sphinganine.

Relative expression of *NMT1*, (N-*myristoyltransferase 1*) was followed at 6 and 48 hpi of *Pst* DC3000 or *Pst AvrRpm1* with or without d18:0. Results are expressed as the fold increase in transcript level compared with the untreated control (0h), referred to as the x1 expression level. Experiments were repeated three times with similar results. Asterisks indicate significant differences between each bacterium co-infiltrated with d18:0 or not (Wilcoxon-Mann-Whitney; *, $p<0.05$).

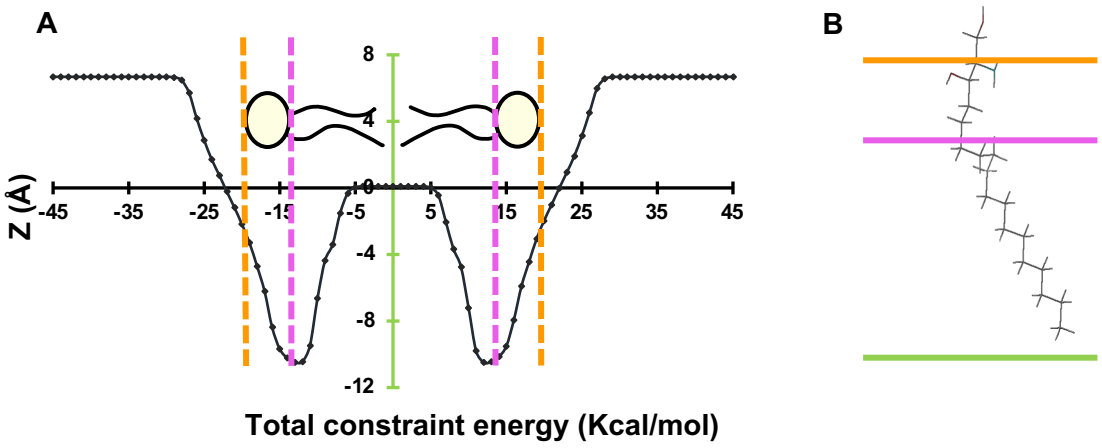

FIGURE 8 Interaction of sphinganine with an implicit modeled bilayer.
(A) The Impala simulation calculates the energy restraints of a lipid bilayer as d18:0 goes through it. The X-axis corresponds to the position of the center of mass along the Z-axis. From left to right: the interface between the bilayer and the aqueous phase (orange), the interface between the polar head and the alkyl chain (pink) and the center of the bilayer (green). (B) The most energetically favorable orientation of d18:0 in the modeled bilayer. The lines represent the same planar surfaces as in A.

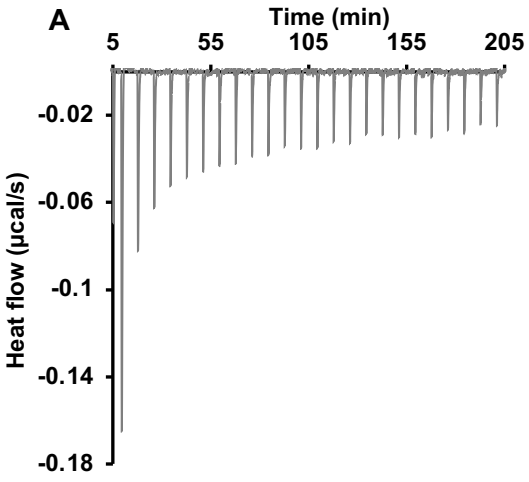

B

	Mean Values	Standard deviations
K (m/M)	86.80	18.99
ΔG (J/mol)	-16.09	0.55
ΔH (J/mol)	-1.39	0.26
TΔS (J/mol)	14.70	0.29

FIGURE 9 Interaction of sphinganine with plant-like liposomes. (A) Raw data from ITC experiments at 26°C. Each peak corresponds to a single injection of a 1 mM PLPC, glucosylceramide and sitosterol (60:20:20, molar ratio) LUV suspension into a solution containing 20 µM of d18:0. (B) Calculated thermodynamic parameters for this interaction. These values are means of two independent experiments. K represents the binding coefficient (the affinity of d18:0 for the LUVs), ΔG represents the molar free energy, ΔH, the molar enthalpy change, and TΔS, the molar entropy change.

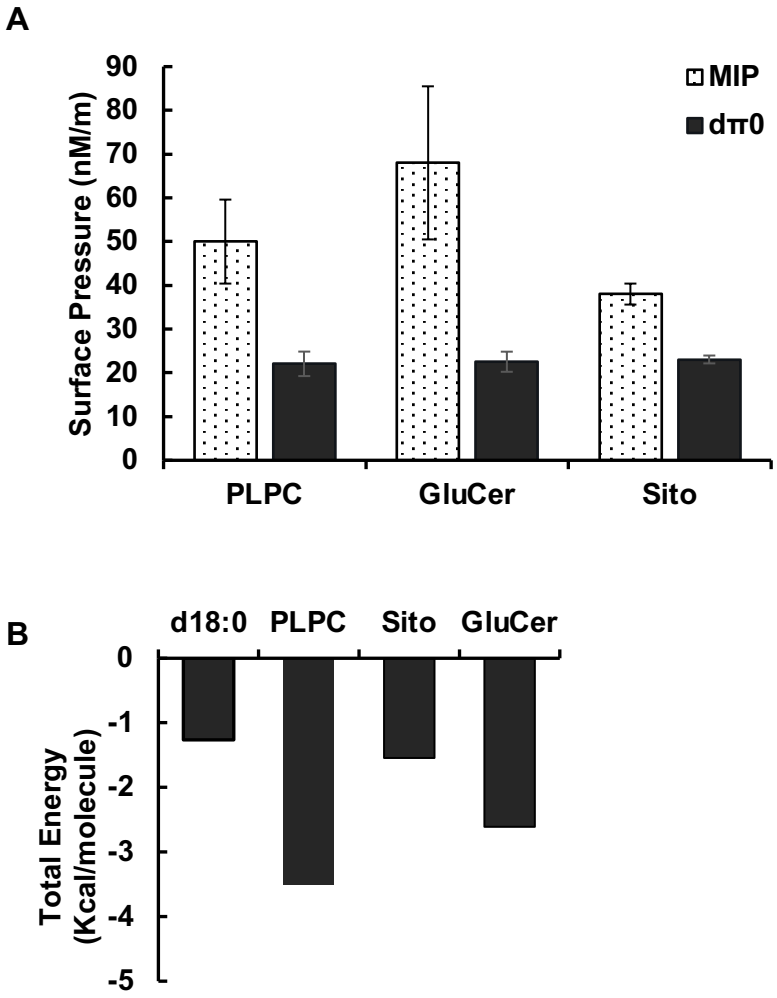

FIGURE 10 Specificity of sphinganine interaction with various lipids representative of the plant plasma membrane.
(A) Adsorption of d18:0 into monolayers of plant PM lipids: PLPC, glucosylceramide (GluCer) and b-sitosterol (Sito). d18:0 was injected at 1.25 μM in a subphase (Tris HCl, 10 mM, pH 7.4), underneath the lipid monolayer. The maximal insertion pressure (MIP) reflects the penetration power of d18:0 into the lipid monolayer and the differential Π (dΠ0) indicates the attracting effect the lipids have on it. (B) Total energies of interaction of d18:0 alone or with lipids representative of the plant plasma membrane were calculated with the Hypermatrix docking method. Lipids used were PLPC, GluCer, and Sito.

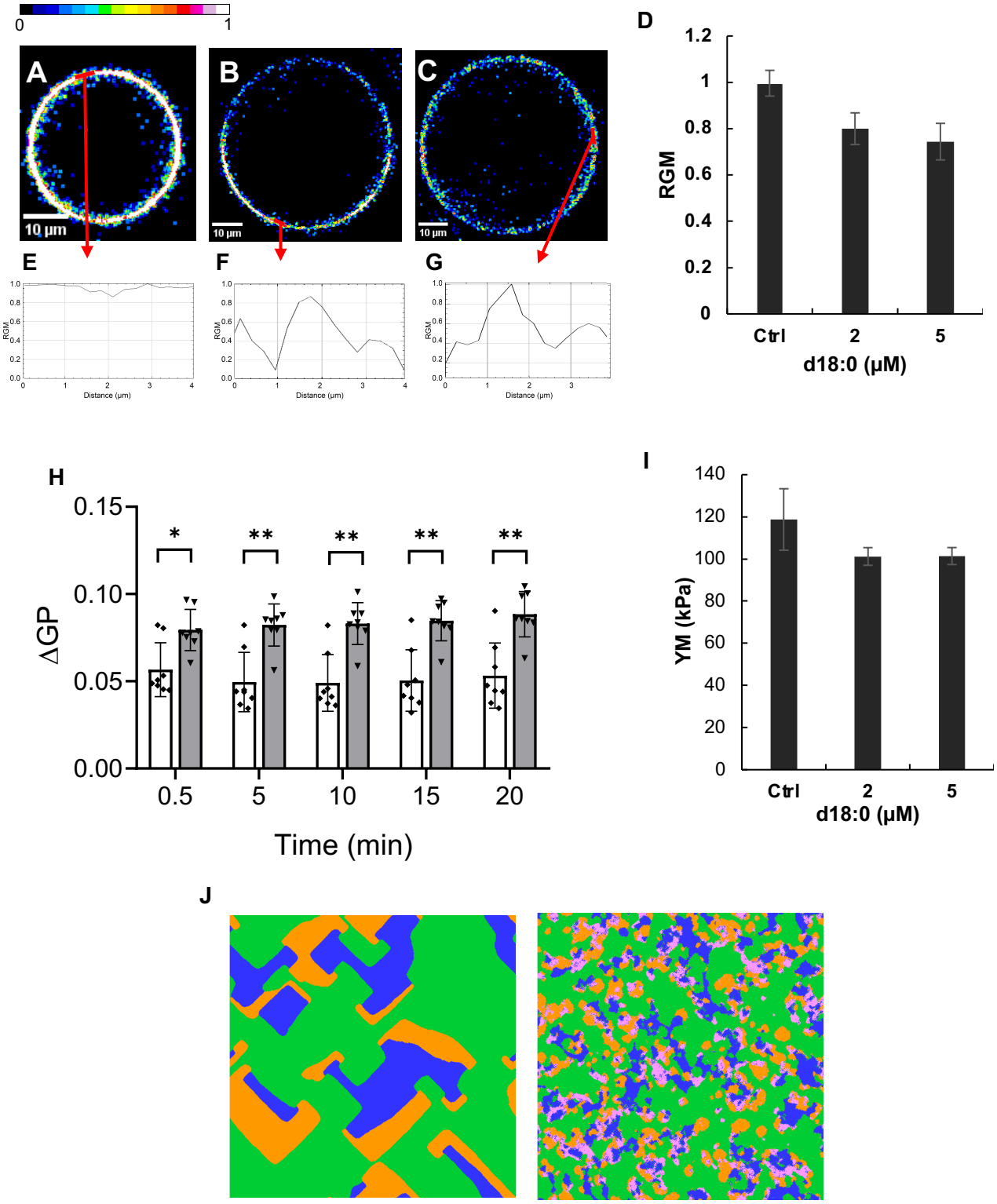

FIGURE 11 Mechanical properties and organization of the plant plasma membrane in response to sphinganine treatment.

(A) to (C) Fluorescence red/green ratio images by multispectral confocal microscopy of a single-cell PM labeled with di-4-ANEPPDHQ after control (A), 2 µM d18:0 (B) or 5 µM d18:0 (C) treatment. (D) Red to green ratio of the PM (RGM) labeled with di-4-ANEPPDHQ treated with control (Ctrl), 2 µM or 5 µM d18:0. The asterisk indicates a significant difference compared to the control (P value < 0.05). (E) to (G) RGM profile on a 4 µm distance on PM from protoplasts after control (E), 2 µM d18:0 (F) or 5 µM d18:0 (G) treatment. (H) Variation of laurdan generalized polarization (ΔGP) measured in PM-mimicking liposomes (50 µM PLPC:Glucosylceramide:β-sitosterol (60:20:20 molar ratio)) at several time points after control (white bars) and 20 µM d18:0 treatment (grey bars). A positive ΔGP corresponds to a higher lipid packing within the bilayer. Mean ± SD of two replicates from four independent experiments. Asterisks indicate statistically significant differences with control, *P<0.05, **P<0.01, two-way ANOVA and Sidak's multiple comparison test. (I) Young's modulus measured on mesophyll protoplasts before or after 5 min incubation of d18:0 at two concentrations. Mean ± SD of at least 50 analyses from three independent experiments. (J) Monolayer simulations of lipid-d18:0 interactions performed with Big Monolayer where each pixel represents a molecule. (Left) Plant lipid model with PLPC in green, glucosylceramide (GluCer) in blue and sitosterol (sito) in orange (60:20:20, molar ratio). (Right) The same lipids after addition of d18:0 in pink (88% lipids, 12% d18:0).